minerals

MDPI

Article

Reduced Viscosity of Mg_2GeO_4 with Minor $MgGeO_3$ between 1000 and 1150 °C Suggests Solid-State Lubrication at the Lithosphere–Asthenosphere Boundary

Thomas P. Ferrand [1,2,*] and Damien Deldicque [3]

[1] Institut des Sciences de la Terre d'Orléans, Université d'Orléans—CNRS UMR-7327, 45100 Orléans, France
[2] Earthquake Research Institute, University of Tokyo, 1-1-1 Yayoi, Bunkyo-ku, Tokyo 113-0032, Japan
[3] Laboratoire de Géologie, CNRS UMR 8538, Ecole Normale Supérieure, PSL Research University, 75005 Paris, France
* Correspondence: thomas.ferrand@univ-orleans.fr

Abstract: Tectonic plates are thought to move above the asthenosphere due to the presence of accumulated melts or volatiles that result in a low-viscosity layer, known as lithosphere–asthenosphere boundary (LAB). Here, we report experiments suggesting that the plates may slide through a solid-state mechanism. Ultrafine-grained aggregates of Mg_2GeO_4 and minor $MgGeO_3$ were synthetized using spark plasma sintering (SPS) and deformed using a 1-atm deformation rig between 950 °C and 1250 °C. For 1000 < T < 1150 °C, the derivative of the stress–strain relation of the material drops down to zero once a critical stress as low as 30–100 MPa is reached. This viscosity reduction is followed by hardening. The deformation curves are consistent with what is commonly observed in steels during the shear-induced transformation from austenite to martensite, the final material being significantly harder. This is referred to as TRansformation-Induced Plasticity (TRIP), widely observed in metal alloys (TRIP alloys). It should be noted that such enhanced plasticity is not necessarily due to a phase transition, but could consist of any kind of transformation, including structural transformations. We suspect a stress-induced grain-boundary destabilization. This could be associated to the transient existence of a metastable phase forming in the vicinity of grain boundaries between 1000 and 1150 °C. However, no such phase can be observed in the recovered samples. Whatever its nature, the rheological transition seems to occur as a result of a competition between diffusional processes (i.e., thermally activated) and displacive processes (i.e., stress-induced and diffusionless). Consequently, the material would be harder at 1200 °C than at 1100 °C thanks to diffusion that would strengthen thermodynamically stable phases or grain-boundary structures. This alternative scenario for the LAB would not require volatiles. Instead, tectonic plates may slide on a layer in which the peridotite is constantly adjusting via a grain-boundary transformation.

Keywords: plate tectonics; lithosphere; asthenosphere; lithosphere–asthenosphere boundary; plasticity; peridotite; mantle; olivine; enstatite; germanates; plate motion; transformation-induced plasticity; transformation; martensitic-like transformation; grain-boundary stability

Plain Language Summary: Alpine skiers glide thanks to the force of gravity, but this could not happen without the transient shear-induced melting of H_2O, which lubricates the sliding. Similarly, tectonic plates move due to slab densification at subduction zones, which generates a driving force throughout the plate, but it is not clear how plate motion actually proceeds. The lithosphere–asthenosphere boundary (LAB) is a low-viscosity layer that seems to accommodate large-scale stresses. Current models consider that the low viscosity of the LAB could be due to partial melting or to the gathering of water or other volatiles. In this study, we present experimental achievements that add an alternative mechanism, requiring neither volatiles nor melting. Tectonic plates may slide on a layer under constant transformation, via a process resembling "cold welding".

check for updates

Citation: Ferrand, T.P.; Deldicque, D. Reduced Viscosity of Mg_2GeO_4 with Minor $MgGeO_3$ between 1000 and 1150 °C Suggests Solid-State Lubrication at the Lithosphere–Asthenosphere Boundary. *Minerals* **2021**, *11*, 600. https://10.3390/min11060600

Academic Editor: Neil M. Ribe

Received: 3 January 2021
Accepted: 28 May 2021
Published: 3 June 2021

Publisher's Note: MDPI stays neutral with regard to jurisdictional claims in published maps and institutional affiliations.

Highlights:

1. A viscosity reduction occurs in ultrafine-grained aggregates of Mg_2GeO_4 and minor $MgGeO_3$, suggesting transformation-induced plasticity.
2. The lithosphere–asthenosphere boundary (LAB) may not result from partial melting or volatiles gathering, but from a solid-state disordering.
3. Tectonic plates may slide on a layer (LAB) in which the peridotite is constantly adjusting via a process resembling "cold welding".

1. Introduction

Plate tectonics is a common process in relatively large terrestrial planets [1] and is strongly related to the origin and evolution of life [2–4]. From the 1960s, the lithosphere and asthenosphere have been defined as the rigid material constituting the tectonic plates and the underlying ductile mantle [5–9]. The term "asthenosphere" was first introduced to designate the sphere of weakness below the lithosphere by Joseph Barrell in 1914 [10,11], and convection beneath oceans was proposed by Arthur Holmes in 1929 [12]. Interrogations about the nature of the lithosphere–asthenosphere boundary (LAB; Figure 1) have recently emerged [13–17]). The LAB is a global feature at a depth separating the lithospheric plates from the underlying asthenosphere. Driven by slab pull at subduction zones (e.g., [18,19]), tectonic plates remain relatively undeformed thanks to decoupling at the LAB [20,21]. Generally considered as a rheological limit between the relatively rigid lithospheric mantle and the more ductile asthenospheric mantle, the LAB may contain melt or volatiles (e.g., [15,22]). However, the LAB is not fully understood yet (e.g., [17,23]), highlighting the requirement of further experimental works.

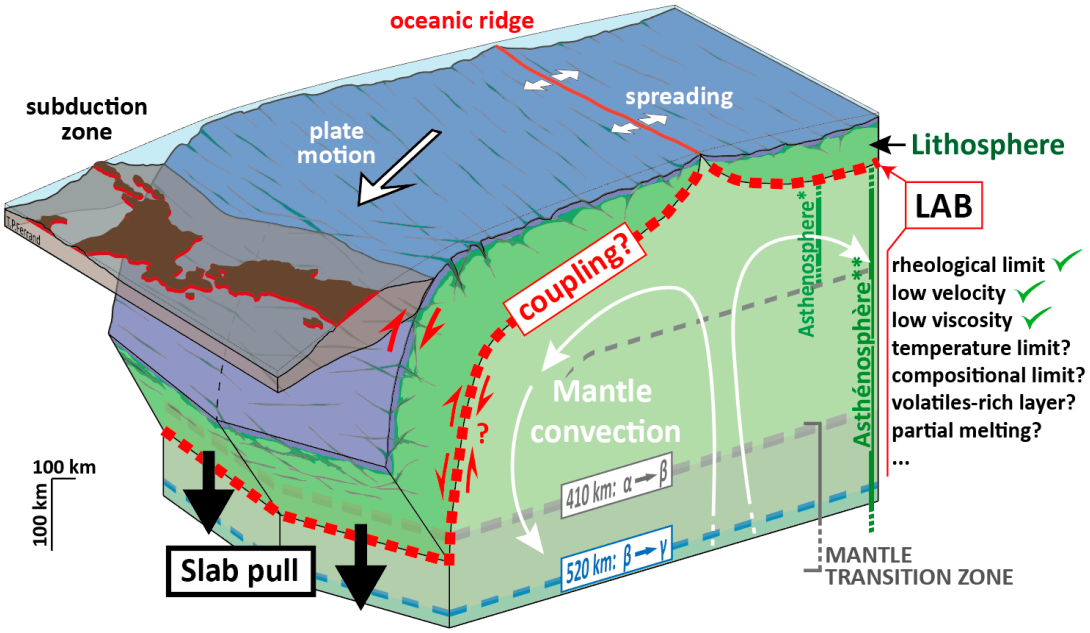

Figure 1. Sketch of the Pacific lithospheric plate focusing on the lithosphere–asthenosphere boundary (LAB). The LAB is a rheological limit that may have its own rheology (Sections 1 and 2). The LAB is usually simplified as a thermal limit at 1260 or 1300 °C and has a standard depth of 80–110 km for ages > 40 Ma. While the overall shear direction is clear at the subduction interface, questions remain regarding the coupling or decoupling between the lithosphere and asthenosphere. For sake of clarity, only the continental crust of the overriding plate is represented. Figure adapted from [24]. For the discussion about the different definitions of the asthenosphere, see Section 5. Vertical exaggeration: ×3.

Tectonic plates are mostly made of peridotite, which constitutes ≈70% of the continental lithosphere (e.g., [25]) and >90% of the oceanic lithosphere (e.g., [26,27]). Hence, the rheology of peridotites is the main parameter that controls plate deformation and motion (e.g., [28]). Natural peridotites mainly consist of olivine and pyroxenes, which are silicates.

Therefore, geophysicists often consider simplified rocks in the MgO-FeO-SiO_2 system for laboratory experiments (e.g., [29–32]). In the State of the Art (Section 2), we recall various mechanisms that have been proposed to account for strain localization at the LAB and its geophysical signatures. Up to date, it is generally accepted that the LAB is characterized by low seismic velocities due to a reduction of viscosity, which could originate from either partial melting and melt pooling [33,34], volatiles [22,35,36], grain-size reduction [37,38], mineral transformations [39,40] and/or grain-boundary disorganization referred to as "pre-melting" [17,41,42]. Using high-pressure deformation machines such as the Griggs apparatus [43,44] or the D-DIA [45–47] is key for the understanding of strain localization at P-T conditions relevant for the LAB. Yet, it has the disadvantage of mixing high-pressure features with textures generated during pressure loading or unloading. Some high-pressure phases are highly unstable at atmospheric conditions and thus cannot be recovered [48,49], and errors in stress measurements at high pressure can make difficult the identification of subtle processes in stress–strain curves. Hence, using germanates instead of silicates may bring complementary insights.

Germanates show striking similarities with silicates and have been studied for more than 60 years (e.g., [50–52]). In particular, the MgO-GeO_2 system exhibits a very similar phase diagram as its natural analogue, the upper mantle (MgO-(FeO)-SiO_2 system; Figure 2) [53,54]. Thanks to very similar properties [55–57], Mg_2GeO_4 has been used in numerous studies as an analogue of $(Mg,Fe)_2SiO_4$ (natural olivine), notably to investigate the rheology of the mantle transition zone (MTZ; 410-660 km depth, Figure 2) and the mechanics of deep earthquakes (e.g., [45,58]). Indeed, when natural olivine (α) transitions to wadsleyite (β) at 410 km (14 GPa) and to ringwoodite (γ) at 520 km (18 GPa), α-Mg_2GeO_4 transitions to γ-Mg_2GeO_4 at 1 atm when T is lowered below 810 °C (Figure 2c). This has allowed to study olivine rheology within the P range of 1-4 GPa, whereas the direct study of natural olivine would have required the use of devices dedicated to much higher pressures. The observations in Mg_2GeO_4 were then reproduced in $(Mg,Fe)_2SiO_4$ in the wadsleyite stability field (14 GPa) [58] and in Fe_2SiO_4 [59]. Similarities were also reported between the pyroxene $MgGeO_3$ (Figure 2d) [54] and its natural analogue $(Mg,Fe)SiO_3$ (Figure 2b) [60].

In this study, we synthetize an analogue of natural peridotites in the MgO-GeO_2 system and deform it 1 atm in order to investigate mantle rheology at LAB conditions, which corresponds to pressures of 2–4 GPa in the natural system.

2. State of the Art: Strain Localization in the Mantle at the LAB

It has been argued that the LAB corresponds to a progressive viscosity reduction (e.g., [61], but seismological observations show a sharp contrast at the LAB [13,23,62] indicating lower seismic velocities than that of both overlying and underlying mantle [23], which seems associated with a lower viscosity [63,64]. In New Zealand, seismological data revealed that both LAB top and bottom correspond to sharp impedance contrasts [23]. If the LAB has its own rheology, a drop of viscosity could indeed result from partial melting (e.g., [33,34]), but also from grain-boundary (GB) pre-melting [17,41]. Olivine, the main component of the upper mantle, is not expected to melt at these P-T conditions, except in the presence of a relatively high H_2O fraction [65]. For pressures of 2 and 3 GPa (≈67 and 100 km), hydrous peridotites can start melting at ≈1300 °C and ≈1400 °C, respectively [66,67]. The corresponding critical H_2O content depends on the rock composition and is estimated between 200 ppm [66] and 450 ppm [67]. Alternatively, pre-melting, i.e., GB disordering in near-solidus conditions promoting diffusion-assisted GB sliding, could explain seismic velocity reduction [42]. Thus, it is reasonable to consider that other transformations could be, like melting, preceded by a solid-state viscosity reduction.

On Earth, collisions never occur between two oceanic lithospheres (e.g., [7,68,69], which suggests that oceanic plates should have the intrinsic ability to maintain their basal stress at relatively low values. Large time and space scales, such as earthquakes cycles, are usually discussed in terms of readjustments of the visco-plastic asthenosphere (e.g., [70]). According to global dynamics modeling, a basal shear stress as low as only 10–100 MPa suffices to allow

decoupling from the convecting asthenosphere [71]. Most recent numerical models of Earth global geodynamics give basal strength values of ≈150 MPa that account for the characteristic scales of current plate tectonics [19]. Seismic anisotropy studies, which nowadays provide the best direct evidence for deformation in Earth's interior, suggest that most of the plate motion is accommodated over a thickness > 100 km (e.g., [72]. Recent numerical modeling also found that the 200-km-thick layer of viscosity reduction, referred to as "asthenosphere" (see discussion in Section 5.3), is probably much thinner, around 100–150 km or less [73], which makes wonder whether this could actually correspond to the LAB. Recent studies present numerical results indicating that the asthenosphere viscosity could be 10 to 100 times smaller than the average upper-mantle viscosity [73,74]. The viscosity of the mantle below the plates is estimated between 3×10^{18} and 10^{19} Pa·s at short time scales (postseismic response) [74,75] and $\geq 10^{19}$ Pa·s for larger time scales [73]. Notably, smaller viscosities after larger earthquakes [74,75] suggest that the viscosity reduction in the asthenosphere is scale-dependent or that enhanced plasticity could happen in response to some stress intensity.

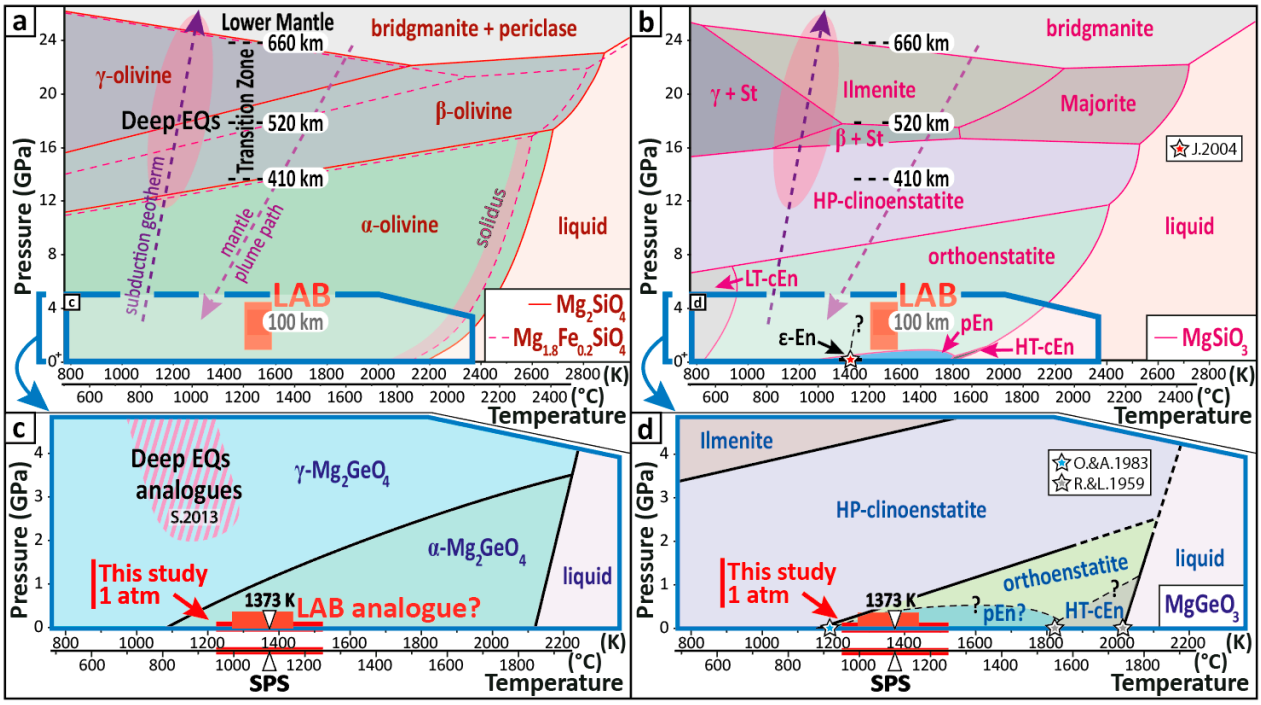

Figure 2. Comparison of $(Mg,Fe)_2SiO_4$ (**a**) and $MgSiO_3$ (**b**) with their analogues Mg_2GeO_4 (**c**) and $MgGeO_3$ (**d**). (**a**) Phase diagram of Mg_2SiO_4 and $(Mg_{0.9}Fe_{0.1})_2SiO_4$ (San Carlos olivine) adapted from [60]. The latter composition corresponds to the San Carlos olivine, extensively studied and considered as representative of the composition of the entire upper mantle. The main discontinuities in the mantle are (1) the lithosphere–asthenosphere boundary (LAB) at an average depth of ≈100 km, (2) the α-β transition at ≈410 km, the β-γ transition at ≈520 km and (4) 660-km discontinuity, i.e., top of the Lower Mantle. (**b**) Phase diagram of $MgSiO_3$ (natural enstatite) [60]. (**c**) Phase diagram of Mg_2GeO_4 (adapted from [76] and [53]) showing the P-T-conditions for deep earthquakes analogues and the P-T range investigated in this study, which may correspond to an analogue of the LAB. (**d**) Phase diagram of $MgGeO_3$ (adapted from [54]) showing the P-T range investigated in this study and the expected stability fields of unquenchable protoenstatite (pEn) and high-T clinoenstatite (HT-cEn). The white cursors indicate the sintering conditions (1100 °C = 1373 K, see text, Figure S1 and Section 3). Legend: St = stishovite; LT-cEn = Low-T clinoenstatite; HT-cEN = High-T clinoenstatite; pEn = protoenstatite; References: O.&A.1983 = [48]; R.&L.1959 = [52]; J.2004 = [49]; S.2013 = [45].

Partial melting at the LAB has been proposed as responsible for plate lubrication [77]. At the East Pacific Rise, magnetotelluric surveys show that the LAB exhibits high electrical conductivity along the spreading direction (8×10^{-2} S·m^{-1}), and significantly lower values parallel to the ridge (3×10^{-3} S·m^{-1}) [78,79]. Such conductivity values and contrast cannot be explained by CPO but could be explained by the presence of small amounts of melt aligned in the spreading direction [80–83]. In this case, because the conductivity

of partially molten rocks is strongly dependent on the geometrical distribution of the melt [84], a high melt connectivity is required [81,83,85]. Shear stress gradients [86] can trigger melt redistribution [87–89]). As a consequence, conductive melt channels constitute a reasonable explanation for the conductive LAB of very young oceanic plates [78,79,90]. Hence, melt-rich channels have been extrapolated to older lithospheres to account for anisotropic electrical anomalies of the LAB (e.g., [16,82,89]), some studies further arguing that the LAB beneath young plates (<25 Ma) would consist of a thin, partially molten layer of low viscosity that would decouple the overlying brittle lithosphere from the deeper convecting mantle [16].However, other parameters are known to significantly increase the electrical conductivity, such as small grain size, which provides a high density of grain boundaries that transport charges [91], and the presence of volatiles that increase this GB diffusion (e.g., [92]). It should also be noted that solid-state transformations can induce electrical conductivity jumps, which was demonstrated during the olivine-spinel transition in the MTZ (>410 km) [93]. In addition, phase transformations induce significant grain size reduction (e.g., [39,94]), which suggests that such structural modification may impact the electrical conductivity as much as melting does [90]. Furthermore, the link between high-conductivity anomalies and the potential presence of melt-rich channels has been seriously questioned by recent experimental results [95] and could be explained by the presence of garnet pyroxenite, i.e., fossilized LAB [90].

H_2O, even in small amounts, lowers the melting point of peridotite by ≈100 °C at least, which for instance, induces partial melting in peridotite around 1300 °C considering San Carlos olivine and 0.32 wt.% (3200 ppm) of H_2O [65]. Considering additional mantle minerals such as pyroxenes and spinel or garnet, it is generally considered that partial melting of hydrous peridotite (1000 ppm H_2O) could be shifted down by ≈200 °C, i.e., 1250 to 1350 °C at pressures between 2.5 and 3.5 GPa [96], i.e., 80–110 km depth (typical LAB for a plate age > 50 Ma). Several studies have discussed the influence of H_2O on the LAB, notably on the partial melting that H_2O would induce (e.g., [14,65–67,96]). Such H_2O saturation is well known at convergent margins, where dehydrating slabs transfer H_2O to the upper plate and cause subduction volcanism (e.g., [97,98]), but it is not clear how H_2O could be trapped at the LAB, which is a global feature. If H_2O is trapped, it would likely remain within hydrous pyroxenites constituting the fossilized early-stage LAB that emplaced near the spreading ridge [90], and the LAB of older plates (e.g., 23 Ma, offshore Nicaragua) likely contains much less H_2O [90]. With lower amounts of H_2O (e.g., 50 ppm) the hydrous solidus is almost equal to the dry solidus, inducing partial melting at temperatures around 1400 °C [96]. In other words, partial melting within the LAB is a matter of debate. Other volatiles have been considered, such as CO_2, leading to the idea that carbonatite melts may exist within the asthenosphere and explain part of its geophysical characteristics (e.g., [81,83]). Nevertheless, if H_2O and/or other volatiles are actually present at the LAB in significant amounts (i.e., 100–1000 ppm), it should have the same consequences as observed in subduction zones, i.e., volcanism. Regarding the global distribution of oceanic volcanism, hydration of the lithospheric mantle in the vicinity of the LAB appears localized and limited (e.g., [99]).

Over the past decades, considerable efforts have focused on quantifying olivine aggregates rheology in terms of flow laws, implemented in geodynamical models for mantle thermal convection (e.g., [71]). Experimental studies investigated the effects of temperature and stress (e.g., [100]), pressure (e.g., [47,101]), volatiles fugacity (e.g., [102]), grain size [37], crystal preferred orientations (CPO; e.g., [29]) and melt fractions (e.g., [103]). The traditional view is to consider one dominant deformation mechanism to given conditions [104]. However, olivine aggregates plasticity involves numerous microscopic mechanisms operating at the same time, within the grains and at grain boundaries [105]. Especially, grain boundary sliding (GBS) has been associated with various mechanisms, either in metals, ceramics or rock-forming minerals [106]. Diffusion-assisted GBS has been evidenced in olivine-rich synthetic peridotites deformed at 1 atm and T > 1300 °C, highlighting the possibility of mantle superplasticity [107]. It should be noted that the diffusion can either

occur at grain boundaries (Coble creep; e.g., [106]) or be intracrystalline (Nabarro–Herring creep; e.g., [108–110]. Dislocation-accommodated GBS has also been evidenced in olivine at low pressure [111,112] and is claimed to be the main deformation mechanism of the upper mantle [113]. In addition, disclinations, evidenced at olivine grain boundaries [114], can accommodate strain. Furthermore, considering relatively low temperatures or relatively high strain rates, local high stress concentrations (e.g., [115]), force chains (e.g., [116]), and stress percolation [117] should be considered. The partitioning between intergranular and intracrystalline high-temperature mechanisms has been quantified at low pressure, notably showing that intergranular mechanisms make olivine aggregates deform 4.6 times faster [118]. Recent experimental achievements demonstrate that grain-to-grain interactions significantly contribute to accommodating strain in synthetic peridotites, suggesting that intergranular plasticity may dominate upper mantle plasticity [105].

Similar investigations have been conducted on pyroxenes (e.g., [119,120]). Notably, the brittle–ductile transition in the flow law of clinopyroxenite at 1.5 GPa has been evidenced not to depend on strain rate for $T < 950$ °C but to strongly depend on strain rate for $T > 950$ °C [121]. Even though pyroxenes tend to be harder than olivine, olivine–pyroxenes aggregates could be significantly weaker [122], especially due to phase mixing [123,124] and associated pinning (e.g., [125]).

As recalled above, until recently, melting was the only "transformation" considered in the interrogations about the LAB reduced viscosity. In this study, based on unexpected experimental results (Section 4), we propose to broaden the discussion (Section 5), including solid-state transformations and potential metastable phases that are not yet fully understood (e.g., [49,52,126]).

3. Experimental Protocol

3.1. Sample Preparation

Fine-grained (~3 µm) aggregates of Mg_2GeO_4 + $MgGeO_3$ (7–8 vol.%) were synthesized from nanosized powders of $Mg(OH)_2$ with average particle size of 50 nm and purity of >99.98%, and liquid tetraethoxygermanium (T.E.O.G.) with a purity of 99.9%. The latter was previously used to synthetize Mg_2GeO_4 [127], as T.E.O.S. is used for the synthesis of silicates (e.g., [128]). We followed the methodology described by [125] up to the calcination step. The overall transformation, depending on the relative amounts of reactive species, is summarized below:

$$\underset{\text{T.E.O.G.}}{Ge(OC_2H_5)_4} + \underset{\text{Brucite}}{2\,Mg(OH)_2} \rightarrow \underset{\text{Forsterite}}{Mg_2GeO_4} + \underset{\text{Ethanol}}{4\,C_2H_5OH} \quad (1)$$

$$\underset{\text{T.E.O.G.}}{Ge(OC_2H_5)_4} + \underset{\text{Brucite}}{Mg(OH)_2} \rightarrow \underset{\text{Enstatite}}{MgGeO_3} + \underset{\text{Ethanol}}{2\,C_2H_5OH} + \underset{\text{Butanol}}{(C_2H_5)_2O} \quad (2)$$

First, brucite, T.E.O.G. and ethanol (solvent) are mixed for 24 h at ambient temperature. Then, the slurry is dried at 60 °C, while stirring continuously with a magnetic stirrer (for a week), until a powder is obtained. The latter is calcined at 1080 °C for 3 h using a box furnace under atmospheric conditions to remove the decomposed products (i.e., H_2O and CO_2). Using a tungsten carbide die, pellets are shaped (cylinders, diameter: 11 mm). These pellets are compacted by cold isostatic pressing at 200 MPa for 10 min (≈25% reduction, diameter: 10 mm). In this study, we used the SPS machine (SPS-110N; Sinterland, Inc., Nagaoka, Japan) installed at the Earthquake Research Institute to obtain the dense and fine-grained aggregate. The sintering technique uses uniaxial loading and pulsed current (DC) under vacuum condition (≈0.4 Pa) for high-speed consolidation of the powder (Figure 3a). The powder was heated to 1100 °C or 1150 °C at a heating rate of 10 °C/min and then held for 20 min under a compressive load of 50 MPa. After the SPS treatment, the applied pressure was reduced below 13 MPa and the specimens were subsequently annealed at 1000 °C for 10 min to relieve the residual strain [129]. The same SPS machine was used in a recent study on diopside [110].

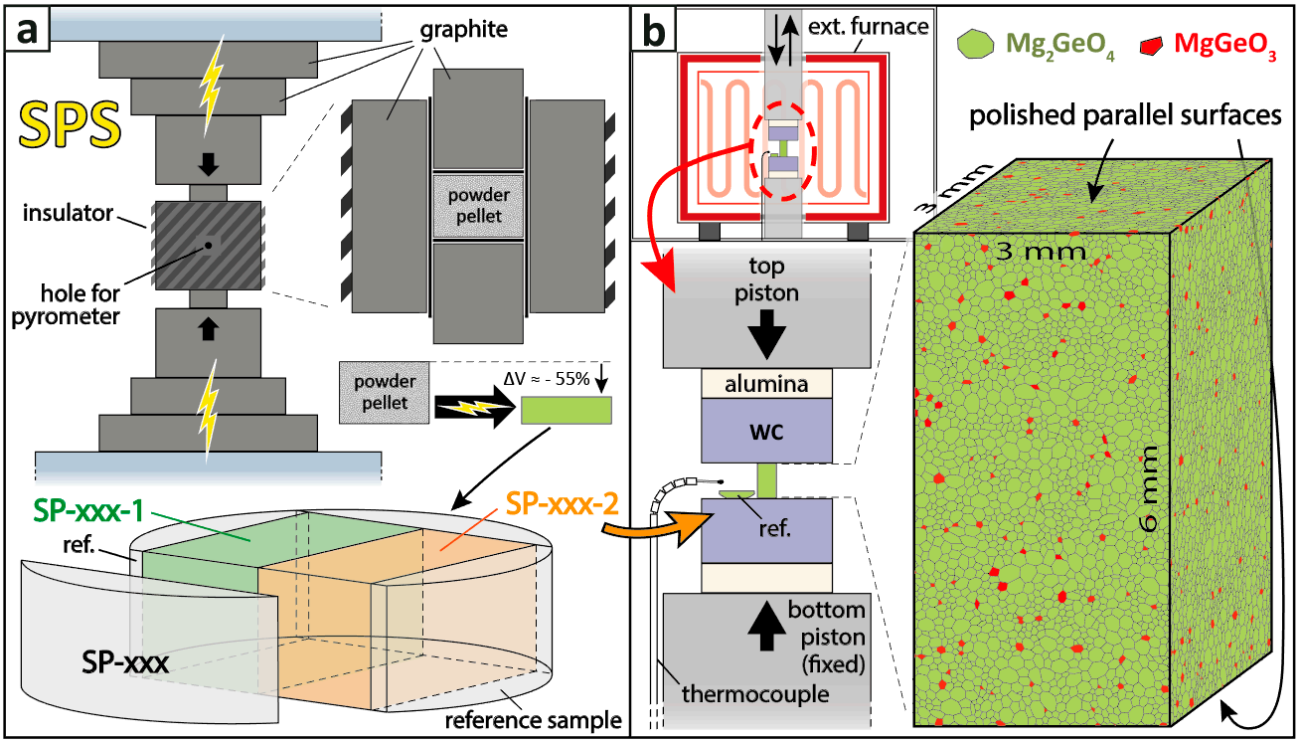

Figure 3. Experimental setup: synthesis and deformation experiment. (**a**) Spark plasma sintering (SPS) and preparation of deformation samples; (**b**) Design of deformation experiments (top left subfigure inspired from [30]) and schematics of a sample before deformation. WC = tungsten carbide.

Phase identification was conducted using XRD (SmartLab 3 kW system, RIGAKU, Japan), confirming that Mg_2GeO_4 and $MgGeO_3$ crystals grow from nanosized particles during SPS (Figure 4). We analyzed the microstructures of samples sintered at 1100 °C and 1150 °C in order to fix the experimental protocol (Figures S3 and S4). The etched surface was coated with a carbon layer of 3–5 nm to prevent charging during microstructure observations using a scanning electron microscope (SEM) equipped with a field emission gun (JEOL JSM-7001F, Nano-Manufacturing Institute, University of Tokyo). At 1100 °C, the aggregates present the smallest grain size and porosity (<0.1 vol.%). Grain size and porosity measurements are described in previous studies [31,125]. A summary of the syntheses is presented in Table S1 and the SPS step is illustrated in Figure S1 and Table S2.

Each SPS sample was cut to obtain samples for two deformation experiments, which consisted of small rectangular parallelepipeds (Figure 3b). The average grain size is ≈3 µm for forsterite and <1 µm for enstatite, as illustrated in Figure 4. Raman and XRD analyses (Figure S2) confirm that the material consists of α-Mg_2GeO_4 with minor ortho-$MgGeO_3$, consistently with most stability studies on Mg_2GeO_4 [53,76]) and $MgGeO_3$ [52,54,130]. However, as recalled in the introduction, some discrepancy exists between experimental studies, some of which reported a metastable enstatite with *Cmca* symmetry (MgO-SiO_2 system) [49], i.e., not protoenstatite (see the discussion in Section 5.1).

The initial purpose of this study was to investigate the behaviour of Mg_2GeO_4. Local mixing heterogeneity would induce the presence of MgO and/or $MgGeO_3$ within the synthetic samples. The rheology of $MgGeO_3$ is relatively comparable to that of Mg_2GeO_4, whereas MgO is significantly weaker and would easily control the deformation. For that reason, $MgGeO_3$ is the phase commonly used as deformation marker within Mg_2GeO_4 samples [45,58]. To avoid residual MgO, T.E.O.G was introduced in excess to get 7–8 wt.% $MgGeO_3$ (≈6–7 vol.%), as in previous studies on mantle rheology [30,31,125,131]. Nevertheless, considering potential underestimated transformations of $MgGeO_3$, the presence of the latter should not be ignored in the interpretation of the mechanical data (see Discussion,

Section 5), as experiments also demonstrated that very small amounts of unstable phase suffice to radically change the rheology of peridotite [46].

High-resolution images of recovered samples were obtained by transmission electron microscopy (TEM; JEOL JEM 2011, 200 kV) at the Université de Paris and crystallographic orientations of Mg_2GeO_4 were obtained by electron backscatter diffraction (MEB-FEG: ZEISS ZIGMA; EBSD: Nordlys Nano, Oxford Instruments) at the Laboratoire de Géologie de l'Ecole Normale Supérieure.

To ensure the observations of this study were not specific to the protocol described above, five additional samples were deformed in the same conditions for comparison (Table 1). HG and PB samples are made of Mg_2GeO_4 and minor $MgGeO_3$, and sample HV consists of Mg_2SiO_4 and minor $MgSiO_3$.

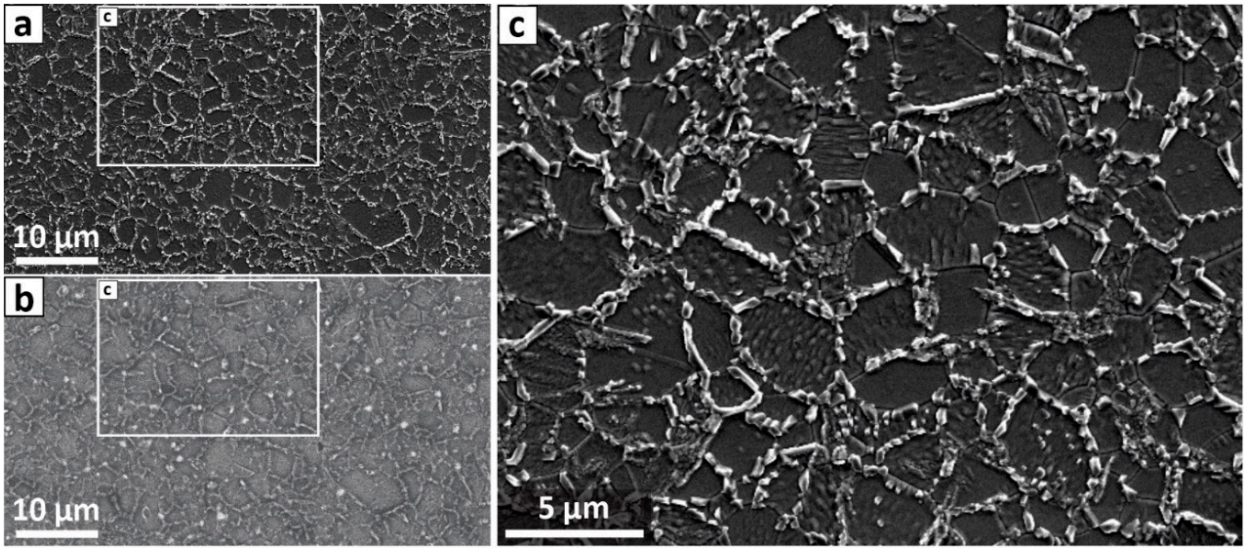

Figure 4. Starting material (SP-307): micrometric Mg_2GeO_4 with minor $MgGeO_3$ (enstatite analogue). Surface polished using micrometric diamond suspension and colloidal silica in the end. Thermal etching at 1020 °C during 30 min. (**a**) Scanning electron microscopy image (secondary electron imaging; SEI) of SP-307, synthetized using SPS and representative of the starting material for all our experiments on Mg_2GeO_4 (Table S1); (**b**) Backscattered electron image of the same area, showing denser crystals in white, corresponding to $MgGeO_3$; (**c**) Closer view (SEI) showing grain growth due to thermal etching. The grain growth is significant at grain boundaries and also noticeable on well-polished grains, reflecting the diversity of crystal orientations. Additional SEM images of SP-307 (homogeneous) and SP-308 (with mixing defects) are presented in Figures S3 and S4, respectively.

Table 1. Description of the samples used for the deformation experiments.

Name.	Major Phase	Fraction	Grain Size	Minor Phase	Fraction	Grain Size	Synthesis
SP	Mg_2GeO_4	92–93 vol.%	3 ± 2 µm	$MgGeO_3$	7–8 vol.%	<1 µm	This study
PB		85–95 vol.%	~30 µm		5–15 vol.%	1–8 µm	[131]
HG		~85 vol.%	~150 µm		~15 vol.%	1–10 µm	[132]
HV	Mg_2SiO_4	91 vol.%	~0.5 µm	$MgSiO_3$	9 vol.%	<0.5 µm	[125]

The preparation of SP samples is described above. Samples PB and HG were provided by Prof. P. Burnley. Sample PB is described in [131] and samples HG correspond to the description provided by [132]. A summary of deformation runs is given in Table S3.

3.2. Deformation Experiments

All the samples described above were deformed in a 1-atm rig, as illustrated in Figure 3b, at a constant temperature, ranging from 940 to 1260 °C (Table S3) using the same uniaxial deformation testing machine (Shimadzu AG-X) with a furnace attached,

installed at the Earthquake Research Institute. The same deformation rig was used in a recent study on diopside [110]. The samples were simply compressed using SiC rods with Al_2O_3 and SiC spacers. A heating of ≈7 °C/min was imposed to the desired temperature for each experiment. The material consists of α-Mg_2GeO_4 with minor ortho-$MgGeO_3$ and both phases are thermodynamically stable in the deformation conditions (Section 3.1). A total of 36 deformation experiments were performed on the synthetic material described in Section 3.1, as well as five additional experiments on materials from other studies (Table 1).

For each sample, a constant strain rate is fixed (from 6×10^{-6} to 3.5×10^{-5} s^{-1}; Table S3) up to a load target, as illustrated on Figure 5 (loading). These strain rates are calculated from the piston advancement and the contact area. The piston speed is fixed to 2 $\mu m \cdot s^{-1}$ for most experiments and reduced to 1 $\mu m \cdot s^{-1}$ and 0.5 $\mu m \cdot s^{-1}$ for additional experiments to study the impact of strain rate on deformation. Once the load target is reached, the load is kept constant, which is referred to as "creep test" in this study, even though the stress is slightly decreasing due to sample widening associated with its shortening.

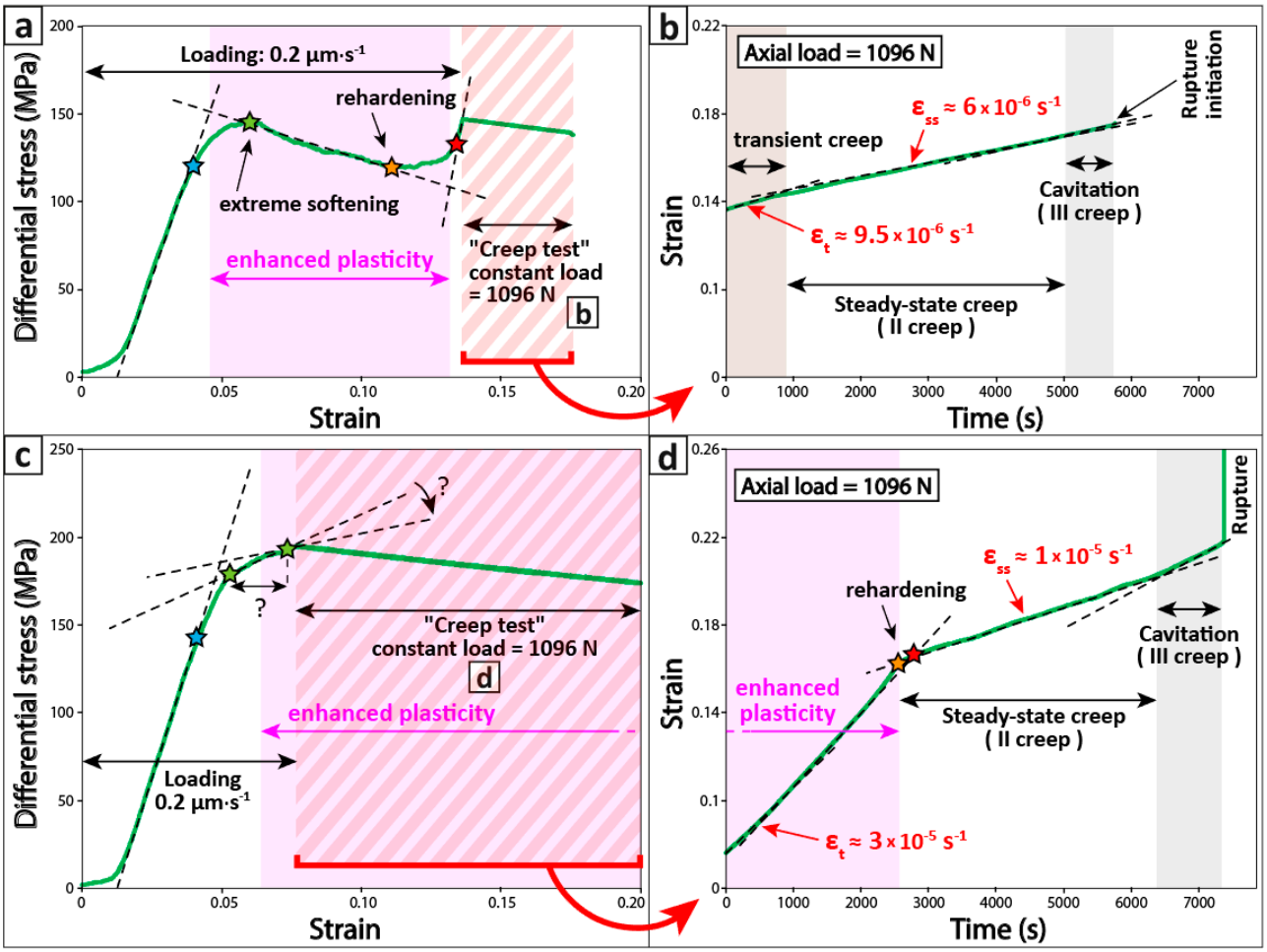

Figure 5. Enhanced plasticity: mechanical data at 1000 ± 7 °C. (**a**) Differential stress as a function of strain for run KG-332 (sample SP-314-2; $\dot{\varepsilon} = 3.17 \times 10^{-5}$ s^{-1}), exhibiting a transient softening during loading; (**b**) Strain as a function of time at a constant load of 1096 N (details in Figure S5); (**c**) Differential stress as a function of strain for run KG-342 (sample SP-322-2; $\dot{\varepsilon} = 3.17 \times 10^{-5}$ s^{-1}); (**d**) Strain as a function of time at a constant load of 1096 N, showing rehardening after ≈40 min of creep. The stars account for the four critical stress values marking the onset of plasticity (blue), the beginning of the linear softening stage (light green), the onset of rehardening (orange) and the beginning of the linear response of the final material (red). Note that the position of the green star in (**c**) is uncertain because of the proximity with the load target and that the orange and red stars are indicated on (**d**). For detailed information, see Section 4.

4. Results: Enhanced Plasticity between 1000 and 1150 °C

The results of the deformation experiments (Figure 3b) performed on SP samples (Figure 4) are presented in this section. Additional experiments on PB, HG and HV samples, are presented in the last paragraph.

Two examples of deformation experiments are presented in Figure 5. Both were performed at 1007 °C and illustrate the variability of the results. A piston displacement of 2 $\mu m \cdot s^{-1}$ was imposed during sample loading (constant strain rate). The stress–strain curve for run KG-332 (Figure 5a) presents an initial viscoelastic response (linear part), followed by a significant softening (negative slope) and finally hardening at ≈ 11% strain, until it reaches ≈150 MPa (load target of 1096 N for a surface of 7.4 mm^2).

Once the load target is reached, it is kept constant and the slightly negative slope in Figure 5a,c means that the sample is slowly widening while shortening. We refer to this part of the experiment as "creep test". In Figure 5b, we show the evolution of strain as a function of time during "creep" (constant load of 1096 N). The strain rate (slope in Figure 5b) is fairly constant and does not exceed 6×10^{-6} s^{-1}, in spite of a slightly faster strain at the beginning of the "creep test" (zoom in Figure S5), known as transient creep, i.e., typical decelerating viscoplastic deformation at the load target (e.g., [133]). In contrast, the stress–strain curve for run KG-342 (Figure 5c) does not present softening, as the stress limit of ≈ 200 MPa (load target of 1096 N for a surface of 5.7 mm^2) is reached before the onset of softening. The strain rate of the "creep test" (Figure 5d) is at first ≈ 3×10^{-5} s^{-1}, i.e., significantly larger than for KG-332, and then drops to 1×10^{-5} s^{-1} at 16% strain for no expected reason. The latter corresponds to the hardening as seen in the case of "creep test" configuration.

During loading at a constant strain rate and 1007 °C (Figure 5a,c), the typical viscoelastic behaviour of $Mg_2GeO_4 \pm MgGeO_3$ is observed [55–57], until the stress reaches its critical value at ≈130 MPa (run KG-332) and ≈150 MPa (run KG-342). This corresponds to the beginning of a softening stage (pink shade in Figure 5), which ends before the load target is reached during run KG-332 and after during run KG-342. The softening is followed by a sharp hardening at 11% and 16% strain, respectively. The difference in critical stress seems to originate from slight differences in strain rate, as this is the only parameter that varies between runs KG-332 and KG-342 during loading. Due to the significant difference in strain at the load target (1096 N; Figure 5a), the contact surface between the piston and the sample differs, and thus the stresses at target are ≈150 MPa and ≈200 MPa, respectively, which influences the steady-state strain rate during the "creep test" stage of the experiment (Figure 5b). For run KG-342, the strain rate keeps a value of ≈3×10^{-5} s^{-1} and then suddenly drops to 1×10^{-5} s^{-1} (Figure 5d). The mechanical data indicate that the rehardening observed during the loading stage of run KG-332 (Figure 5a) is observed during the "creep test" stage of run KG-342 (Figure 5d). It should be noted that the change in strain rate is much larger and sharper than what is commonly observed during the abovementioned transient creep. In addition, the final material tends to be harder than the initial material. Once the softening stage is finished, the material exhibits a constant steady-state strain rate, until strain-induced cavitation (i.e., tertiary creep) drives strain acceleration and the coalescence of the cavitation leads to macroscopic fracture of the sample.

The germanate samples were deformed at fixed temperatures ranging from 900 to 1250 °C (Figure 6). Experiments at various temperatures reveal that the critical stress is strongly temperature-dependent, decreasing with temperature as long as $T < 1150$ °C (coloured curves) and then increasing with temperature for $T \geq 1050$ °C (grey curves). The plasticity begins at stresses ≈ 60 MPa at 1054 °C and at stresses as low as 20 MPa for T ≈ 1100 °C. Then, due to enhanced plasticity with increasing temperatures, the load target (1038 N in Figure 6) is reached at decreasing stress values, from ≈115 MPa at 1054 °C down to ≈85 MPa at 1100 °C. Most surprisingly, at ≈1150 °C the material is harder and at higher temperatures the enhanced plasticity is no longer observed (Figure 6a). The comparison of the strain rates during the constant-load stage confirms that the material is harder once the stage of enhanced plasticity ends (Figure 6b). It should also be noted

that the steady-state strain rate significantly increases with temperature between 1150 and 1200 °C (Figure 6b). The dataset presented in Figure 6 suggests that the enhanced plasticity only occurs within a temperature window, as illustrated for the entire dataset in Figure 7.

The entire dataset (36 deformation tests; Table S3) is presented in Figure 7, showing the derivative of the stress–strain relation (i.e., slope of the stress–strain curve) as a function of temperature (constant for each experiment). It confirms that the enhanced plasticity occurs within a narrow temperature window, which limits appear to depend on strain rate (Figure 7). The stage of enhanced plasticity is tentatively referred to as "TRIP" for "TRansformation-induced plasticity" in Figure 7 due to the similarity between the mechanical data and what is commonly observed in TRIP alloys (e.g., [134–137]). Importantly, the "transformation" is not necessarily a "phase transformation". Its nature is discussed in Section 5.1.

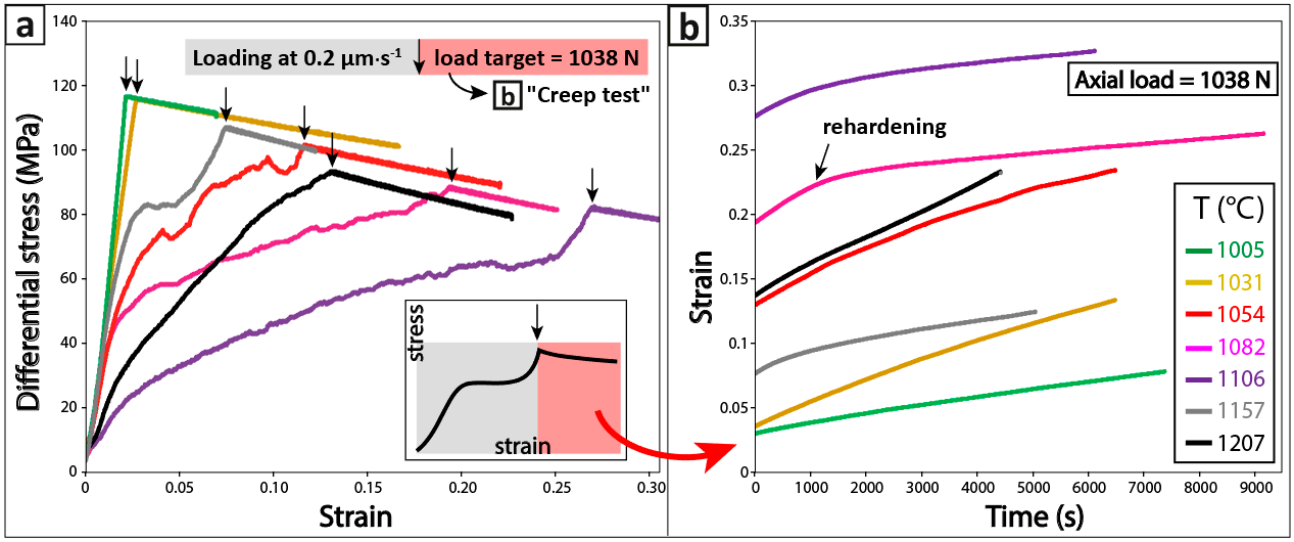

Figure 6. Set of experiments for a loading rate of 0.2 µm·s^{-1} up to 1038 N. (**a**) Stress as a function of axial strain during the loading step (grey shade) and the creep test (red shade), for temperatures between 1005 and 1207 °C; (**b**) Strain as a function of time at a constant load of 1038 N. Vertical arrows on (**a**) account for the load target, i.e., beginning of the "creep test" (**b**).

Critical stress values can be defined at transitions between deformation stages, as illustrated in Figure 8 (inset). The values of the critical stress also highlight the temperature window in which the enhanced plasticity occurs (Figure 8), with a systematic decrease of critical stresses with increasing temperature for $T \leq 1100$ °C. In any case, very low strength is observed for $T \approx 1100$ °C (Figures 7 and 8). The "creep test" parts of the experiments (Figure 5b,d and Figure 6b) are summarized in Figure 9. Depending on whether or not rehardening occurred during loading, the strain rates at the load target (Figure 9a) and during steady-state deformation (Figure 9b) significantly differ. For low load targets ("creep tests" with $\sigma_{max} < 60$ MPa), strain rates increase with increasing temperature, exhibiting stress exponents n either >2 (e.g., 1100 °C, $\sigma < 20$ MPa) or ≈1 (e.g., 1000 °C, $\sigma < 20$ MPa). However, experiments with high load targets reveal a complete disorganization of the temperature dependence (Figure 9). The transient enhanced plasticity stage corresponds to a change in the main deformation mechanism, especially visible for the set of experiments performed at ≈1500 °C, which exhibits a negative apparent stress exponent (Figure 9b). Previous studies on $Mg_2GeO_4 \pm MgGeO_3$ in similar conditions but with larger grain sizes provided stress exponents n ≈ 2 [55,56] to n ≈ 3 [57], suggesting a deformation controlled by dislocation creep. The particularity of our study is the very small grain size, which is known to favour diffusion-assisted grain-boundary sliding (n ≈ 1) instead of dislocation creep (n ≈ 3), as documented and discussed by numerous studies (e.g., [37,105,107,110,118]).

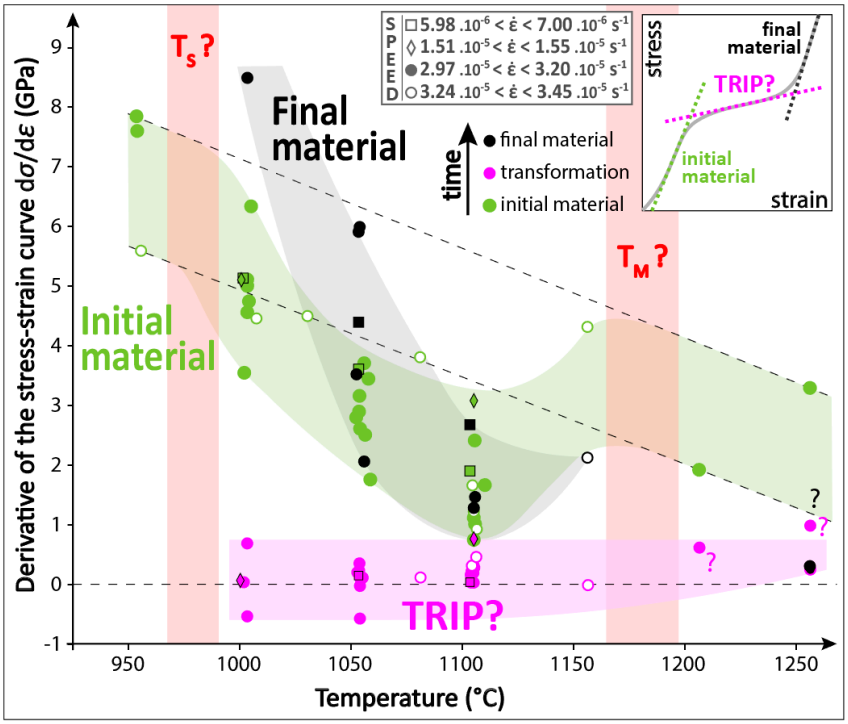

Figure 7. Slope of the stress–strain curve as a function of temperature. The observed enhanced plasticity is characterized by an average plastic response with $d\sigma/d\varepsilon \approx 0$, which suggests TRIP. Considering the analogy with a martensitic-like transformation (see Section 5.1), T_S and T_M would account for the starting temperature and martensitic temperature, respectively, which would define the "martensitic window", i.e., domain where the enhanced plasticity is observed. Temperature variation during loading is <6 °C.

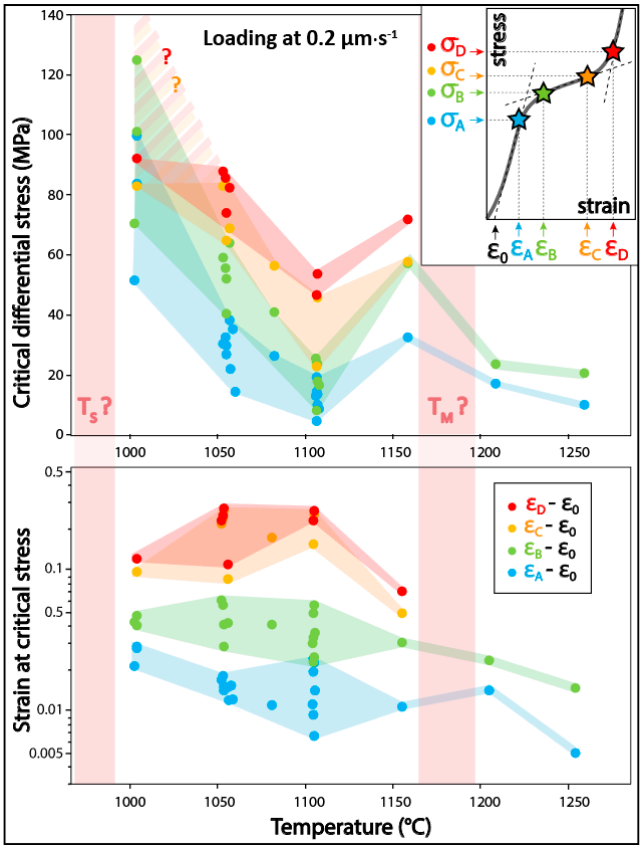

Figure 8. Critical differential stresses and associated strain. The "martensitic window", between T_S and T_M, is defined in Figure 7.

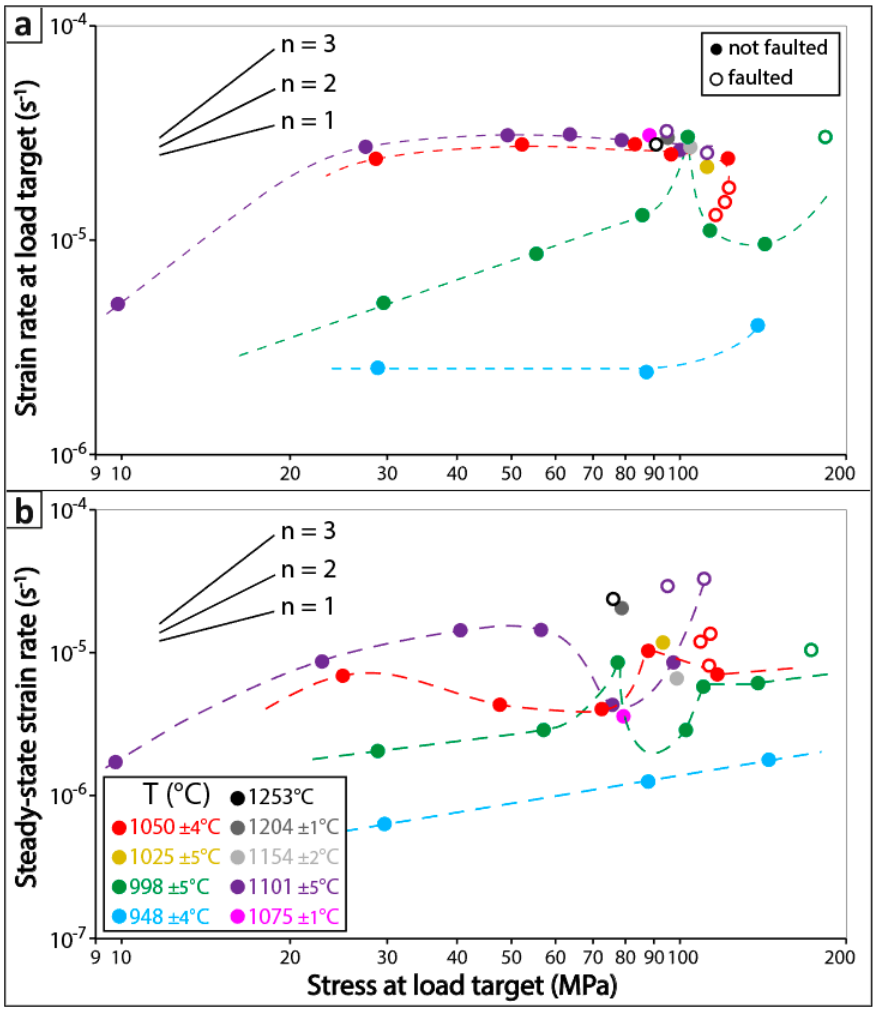

Figure 9. Results of creep tests. (**a**) Strain rate right after the load target is reached; (**b**) Strain rate once the secondary creep reaches a steady state. Solid and open circles account, respectively, for samples that deformed homogeneously until the end of the experiment and samples in which tertiary creep (cavitation) eventually lead to macroscopic faulting. Stress exponents are indicated for comparison with other diffusion- and dislocation-dominated deformation mechanisms (see text). The Temperature variation during each experiment is lower than 5 °C.

Observations by TEM on FIB sections (focused ion beam; Figure 10) at olivine grain boundaries reveal well-preserved triple junctions (Figure 10a), contrary to what is observed in the case of cavitation at grain boundaries in materials such as tungsten [138]. Along certain grain boundaries, microstructures compatible with GBS were identified (Figure 10b), whereas other grain boundaries seem to exhibit crenulations (Figure 10e). Most surprisingly, aggregates of nanometric grains were identified squeezed in gaps between straight grain boundaries, which may consist of recrystallized material or GBS-induced shavings (Figure 10g–h) and are not associated with amorphization (Figure 10i). In addition, EBSD measurements (Figure 11) show that the olivine grains exhibit a CPO with the b-axis parallel to σ_{max}, which would be consistent with high-temperature GBS [111].

Because the enhanced plasticity and associated rehardening described in this study are unexpected and puzzling, additional experiments were performed on other germanate samples (Section 3). The results of these additional experiments are presented in Figure 12: a moderate stress at a load target (150 MPa) in HG samples [132] does not induce enhanced plasticity (Figure 12a), but higher stresses do (Figure 12b). In addition, the sample from Burnley et al. [131] exhibits a much lower critical stress, with enhanced plasticity occurring at stress levels similar to our SPS samples. The enhanced plasticity is confirmed, but

for higher critical stresses in case of larger grain size, which suggests that the enhanced plasticity mechanism is grain-size-dependent.

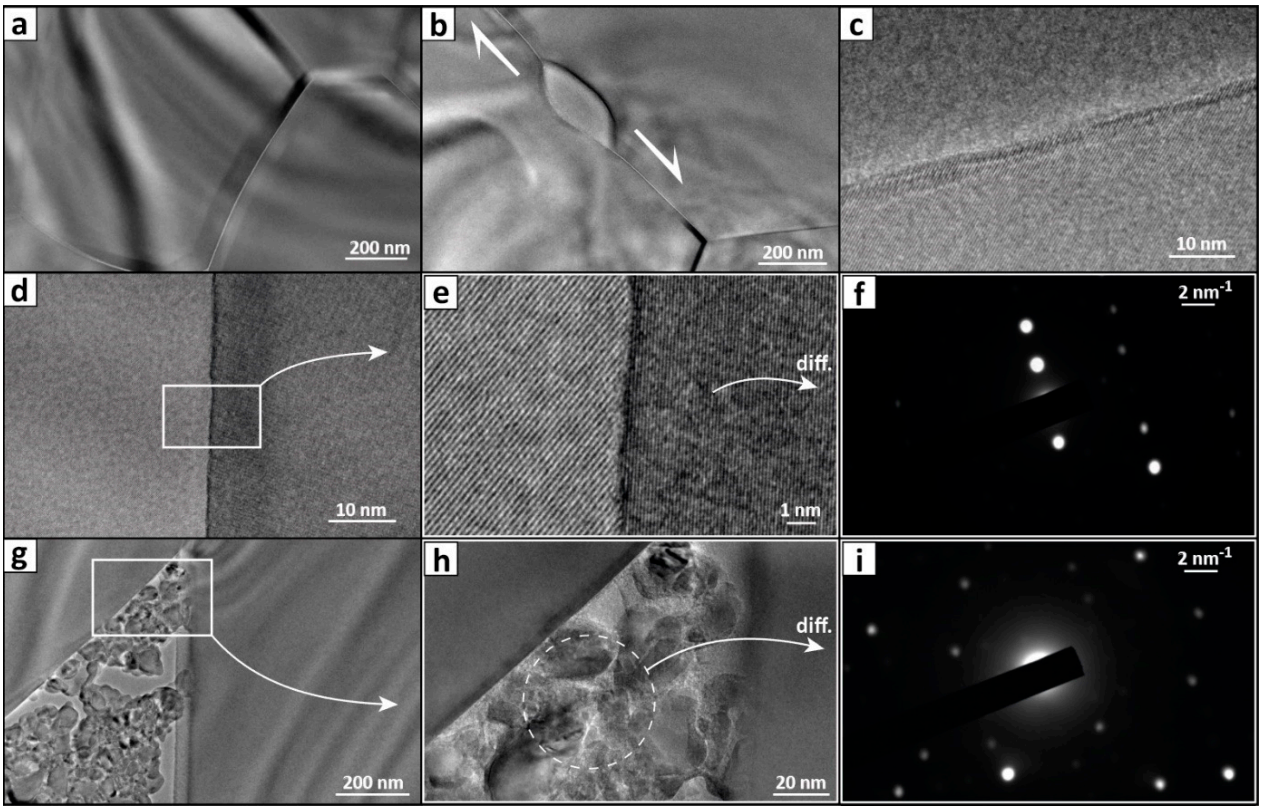

Figure 10. Transmission electron microscopy (TEM) images of the sample SP-309-1 (run KG-320). Sample deformed at 1050 °C and >100 MPa; (**a**) micrometric Mg_2GeO_4 crystals exhibiting well-preserved triple junctions; (**b**) Interstitial nanometric grain likely highlighting GBS (white arrows) and triple junction; (**c**,**d**) Representative grain boundaries between micrometric olivine grains, which do not exhibit any dislocation; (**e**) Closer view on the grain boundary (**d**); (**f**) Electron diffraction pattern of a micrometric grain of olivine; (**g**) Aggregate of nanometric grains squeezed in a gap between two straight grain boundaries after GBS; (**h**) Closer view on the aggregate; (**i**) Electron diffraction pattern of the nanograined aggregates, showing the absence of amorphous material.

5. Discussion

In this study, we document an enhanced plasticity of a peridotite analogue in the MgO-GeO_2 system at 1 atm between 1000 and 1150 °C, followed by a sharp hardening. The mechanical data demonstrate that, within this temperature window, the derivative of the stress–strain relation of the material drops down to zero once a critical stress as low as 30–100 MPa is reached (Figure 7), and that this critical stress is minimal around 1100 °C (Figure 8). The data are consistent with a "transformation" similar to what is commonly observed in steels and shape-memory alloys during the shear-induced transformation from austenite to martensite, the final material being significantly harder. The nature of the "transformation" is addressed in Section 5.1. TRansformation-induced plasticity (TRIP) is well known in "TRIP alloys" (e.g., [137,139]) and highly related to the concept of superplasticity (e.g., [107]), as discussed in Section 5.2.

5.1. The "Transformation": A Transient Metastable Phase Responsible for Enhanced Plasticity?

Among all the observations presented and discussed above, the rehardening following the stage of enhanced plasticity suggests that a "transformation" is taking place and that this hardening corresponds to the end of the transformation. The mechanical data presented in this study (e.g., Figure 5a) resembles the typical stress–strain curves of TRIP

alloys (e.g., [134–137,140]). Strain hardening has been described in various steels enduring TRIP, notably associated with dislocation activity (dislocation strengthening) due to the martensitic transformation of retained austenite [141]. Depending on the steels, the observed rearrangement of dislocations has been described either as a displacive, diffusionless mechanism [137] or as a diffusion-type mechanism [142]. Such hardening is also well understood during twinning mechanisms in metal alloys [143–146]. Cold welding, well known in metals (e.g., [147,148]) and also evidenced in ceramics [149], is strongly related with lattice reordering and TRIP (e.g., [137,150]).

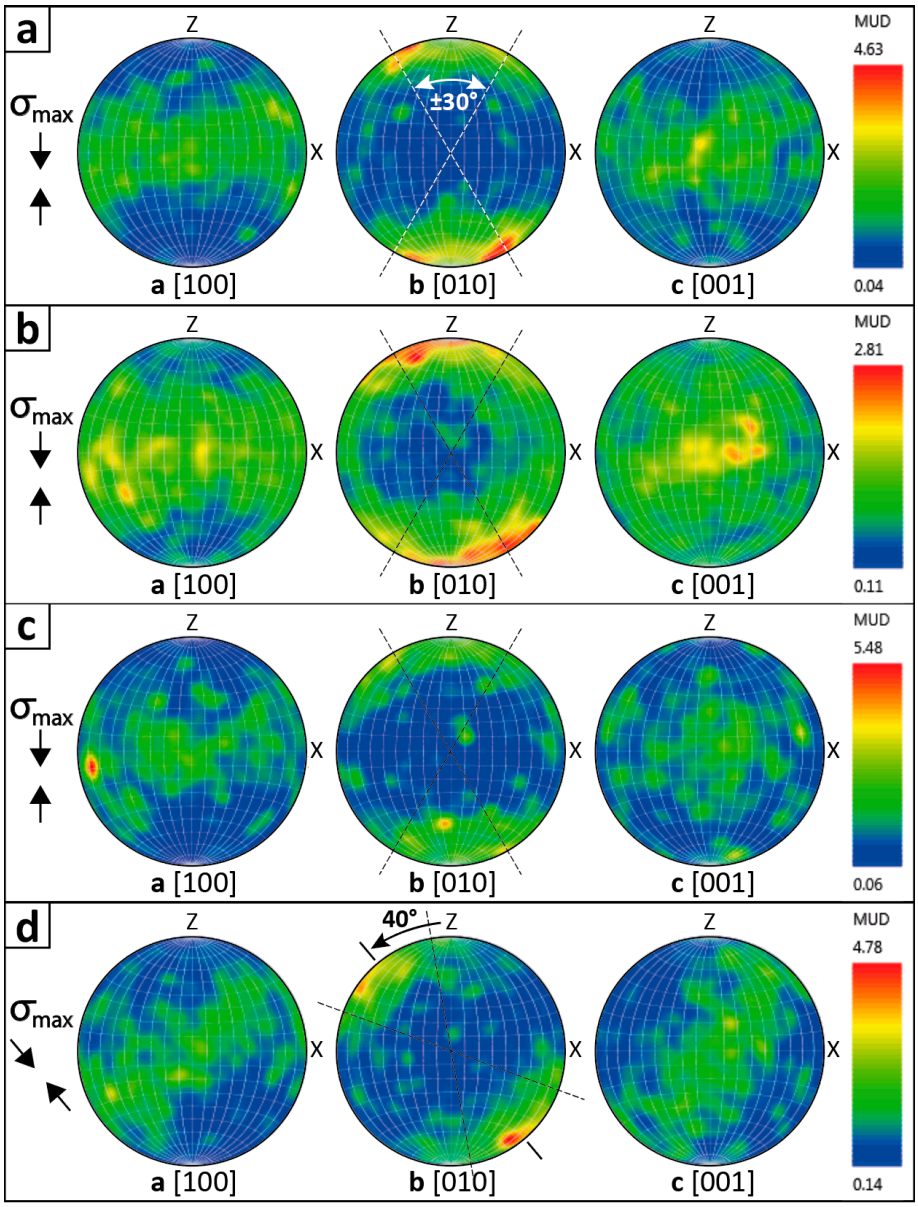

Figure 11. Electron backscatter diffraction (EBSD) pole figures on deformed samples. (**a**) Run KG-329, starting material SP-313-1, T = 1002 °C, σ_{max} = 110 MPa (15,793 analysis points); (**b**) Run KG-322, starting material SP-310-1, T = 1056.5 °C, σ_{max} = 55 MPa (33,402 analysis points); (**c**) Run KG-330, starting material SP-313-2, T = 1105.5 °C, σ_{max} = 105 MPa (29,215 analysis points); (**d**) Same as (**c**) but data collected near a corner of the sample, where the stress field turns with σ_{max} oriented ≈ 40° from the vertical axis (80,078 analysis points). In any case, the b-axis tends to orient in a direction ± 30° to the compressive stress. Upper stereographic projection. MUD = multiples of uniform distribution. Indexation: 55–80% (≈99% Fo + ≈1% oEn). The Z direction is parallel to σ_1. Lower hemisphere. For acquisition conditions, see Table S4.

The increase in transformational strain with decreasing grain size commonly indicates the importance of GB effects, such as the occurrence of GBS [151]. In this study, the additional experiments performed on similar material with larger grain sizes (Figure 12) would highlight the grain-size dependence of this TRIP, which would operate via diffusion-assisted and/or transformation-assisted GBS. Both the microstructural observations (Figure 10) and the CPO (Figure 11) would be consistent with such GBS. Notably, TEM imaging (Figure 10) reveals dislocation-free crystals as well as nanomaterial squeezed between certain straight grain boundaries. Importantly, it should be recalled that both transformation and structural superplasticity exist (e.g., [151]). The latter corresponds to a drastic increase in material ductility under restricted conditions (e.g., [152,153]). Superplasticity is usually evidenced in tension experiments (e.g., [107]) allowing >100% strain, whereas the samples deformed in the study only reach ≈ 30% strain in compression with a pure shear design. Discussing processes, this distinction can be extended to TRIP. Considering structural superplasticity, several mechanisms mentioned in Section 5.2 could be involved. Especially, GB reordering (CPO formation) due to a change in the dominant slip-system is a good candidate for accommodating grain-scale elastic strain during GBS.

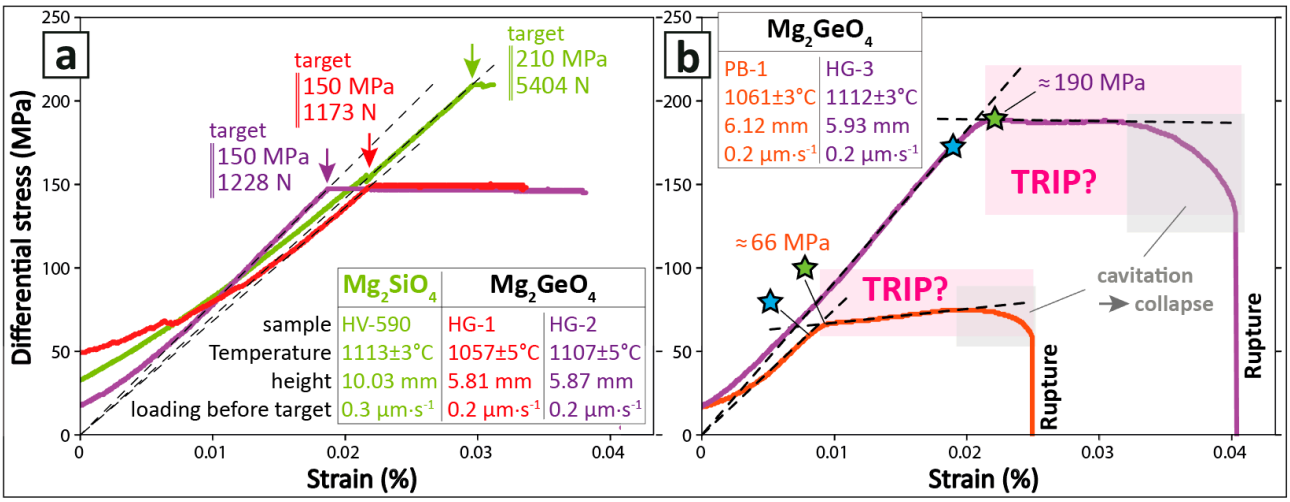

Figure 12. Additional experiments on Mg_2SiO_4 (+$MgSiO_3$) and Mg_2GeO_4 (+$MgGeO_3$) samples from other studies. (**a**) Experiments that do not exhibit enhanced plasticity; (**b**) Enhanced plasticity (load target never reached) reproduced in germanate samples synthetized for previous studies, which we propose to interpret as TRIP. All samples contain minor enstatite (Table 1). Samples 'HV', 'HG' and 'PB' are respectively described by [125,131,132]. See the signification of the blue and green stars in Figure 6.

The nature of the "transformation" occurring in germanates is a matter of debate. Using either SEM imaging, Raman spectrometry, XRD or EBSD analyses, no convincing trace of any metastable phase was evidenced in the recovered samples, which does not necessarily mean that such phase did not transiently form. In low-carbon low alloy steels, high-strain-rate superplasticity was evidenced to be due to a dynamic reverse phase transformation [154]. Such reverse transformation could apply either for a proper phase transition or for another kind of "transformation" such as pre-melting or other GB disordering (Section 5.2). Metastable phases are difficult to observe or reproduce in the laboratory, and thus often underestimated; yet, some studies suggest that transient phases [155,156] or grain-boundary instability [40,157] could be responsible of enhanced plasticity.

As far as we know, both above and below the LAB, chemistry and thermodynamics considerations would indicate that the mantle is made of α-olivine with minor pyroxenes and garnet, with possibly large variability of the proportion of these "minor" phases. The low-velocity layer at the bottom of the lithospheric plates (LAB) should also consist of this material. As recalled in the State of the Art (Section 2), strong seismic reflectors can be observed at both the top and bottom of the LAB in New Zealand [23], suggesting sharp

viscosity contrasts, with significantly lower seismic velocities within the LAB compared to both the lithosphere and the asthenosphere. Such low-velocity zone (LVZ) can be at least as wide as 70 km (60–130 km depth range) [62]. Here, we argue that possibly unknown or underestimated phase transformations could be responsible for the enhanced plasticity evidenced both in the lab and within the LAB.

For comparison, recent experimental achievements suggest that a transitional phase could play a role in the rheology of the MTZ [155], i.e., where phase transformations occur. Following an earlier suggestion by Gordon [158], Sammis and Dein [159] examined the possibility that the transforming zone (MTZ) has a low effective viscosity due to transformation superplasticity. Poirier [160] suggested that olivine was a martensitic material and that an intermediate "martensite", known either as ε*-olivine (e.g., [160]) or as ω-olivine (e.g., [161]), should transiently exist during the olivine-spinel transition within relatively cold subducting slabs ($T < 1100$ °C). This phase has recently been found within ringwoodite meteorites [126] due to fast coeval cooling and decompression right after the impact. In such materials, martensitic transformations can be induced by either changing the temperature (on cooling) or applying differential stress (e.g., [162,163]).

Metastability is often called on to explain delays or spatial shifts between nominal minerals and observations of natural systems, for example regarding serpentine minerals, which is inappropriate as metastability is actually mistaken for variations in composition, structure, fluid saturation, percolation, O_2 fugacity and/or oxidation state [32,164]. Yet, numerous minerals can be metastable, e.g., metastable olivine involved in deep earthquakes (e.g., [45,59,165]). Furthermore, some phases do not have any stability field in a P-T diagram, such as ω-olivine (e.g., [126,160]), which could have a stability field in a P-T-σ diagram. Thus, the ω-olivine is an example of metastable phase, and, even though it is not expected to exist in the conditions investigated in this study, it should be taken into account regarding the composition of the experimental samples (i.e., 93% olivine).

The transient existence of a stress-induced metastable olivine could be considered among the processes that could account for the observed enhanced plasticity. The ω-olivine would transiently form through stacking faults during α-β-γ transitions (e.g., [126,166]). Theoretical developments demonstrate that the shear modulus of the involved slip systems should decrease considerably near the transition [160], necessarily inducing TRIP. Experiments on Fe_2SiO_4 have revealed cation disordering associated with the α-γ transformation followed by a delay in cation reordering [167]. This two-step mechanism was described as pseudomartensitic [167,168]. In material science, such cation disordering, associated or not with further transformation, is referred to as premartensitic transition (e.g., [169,170]). In addition, during the transition from olivine (α) to wadsleyite (β) and ringwoodite (γ), time-resolved XRD allowed to identify an intermediate phase in which the oxygen exhibits a spinel lattice but cations are disorganized and reorganize later by short-distance diffusion [171–173], which is very consistent with the abovementioned observations in Fe_2SiO_4 [167]. Ultrasonic measurements under synchrotron radiation suggest an effect of the intermediate phase on the seismic velocities and attenuation that could affect the 410-km discontinuity signature [155]. We argue that if such mechanism is proposed to explain the LVZ at the 410-km discontinuity, it (or part of it) should also be discussed regarding the LAB.

Olivine is thermodynamically stable at P-T conditions relevant for the LAB (Figure 2a), whereas pyroxenes might not be [48,49]. Thus, transformations of the latter may seem more likely. Over the past decades, numerous phases that are not stable at ambient temperature and atmospheric pressure have been discovered, some of which described as unquenchable (e.g., [49,52,174]). In particular, $MgSiO_3$ protoenstatite has a restricted stability field (Figure 2) but has been described as metastable (e.g., [175]). Another possibility could be the transition from orthoenstatite to *Cmca*-enstatite [49]. The latter was described as a consequence of a displacive phase transition, observed at temperatures above 1090–1175 °C and up to 1350 °C at least [49] (called "ε-En" in Figure 2b for consistency). In the MgO-GeO_2 system, a "clino-from-proto" phase was described [48], i.e., protoenstatite ghosts characterized by

newly formed clinoenstatite in recovered samples. Because such unstable phases transform back during the quench, complementary in-situ measurements are required, which is one of the reasons why synchrotron experiments have become so popular (e.g., [167,168]). In the experiments of Ozima and Akimoto [48], the protoenstatite is described as unquenchable, which is actually not the case in the MgO-SiO_2 system. Thus, we propose that the unquenchable $MgGeO_3$ phase evidenced by Ozima and Akimoto [48] may be the analogue of the unquenchable $MgSiO_3$ crystals identified by Jackson et al. [49]. We propose unknown/underestimated transitions in (Mg,Fe)SiO_3 as alternative sources for the enigmatic low viscosity allowing plate motion. One could imagine that the pyroxene fraction of mantle rocks could control plate velocities and explain why some plates move faster than others.

Whether or not the abovementioned metastable phases actually form during peridotite shearing at LAB conditions is unclear. The unexpected enhanced plasticity observed in the MgO-GeO_2 system and potentially responsible for the LAB low viscosity is most probably due to a general disorganization of grain boundaries within a restricted P-T window (Section 5.2), and the potential occurrence of a phase transition would definitely drive such GB disordering. Finally, one could argue that our results question the use of Mg_2GeO_4 as an analogue for deep natural olivine: either this behaviour is specific to the MgO-GeO_2 system and the analogy is limited, or natural peridotites also endure enhanced plasticity in certain P-T conditions that remain unknown up to date.

5.2. Plate Lubrication without Partial Melting at the LAB?

The presence of a melt/fluid fraction that would be characteristic for the LAB has become the basis for interpretations in numerous studies (e.g., [16,23,62]). Beneath the East Pacific Rise, indeed, the high conductivity values observed in the vicinity of the LAB (e.g., [78]) can be explained neither by olivine hydration [176] nor by garnet pyroxenite channels [90]. Conductivity values $\geq$ 0.1 $S.m^{-1}$ at 50–100 km depth require >300 wt. ppm H_2O in olivine, implying >1000–1500 wt. ppm H_2O in an equilibrated peridotite [176], which is well above the 0–200 wt. ppm at which peridotite starts melting at these depths [66].

Models considering an anisotropic melt distribution perpendicular to the ridge allow to reproduce the observed conductivity data for young oceanic plates (<5 Ma) [78]. Regarding the 20–25 Ma Cocos Plate offshore Nicaragua, garnet pyroxenites best explain the anisotropic conductive anomaly at 40–60 km depth, but local melt pooling could well explain another anomaly at about ≈100 km depth [90]. In addition, magnetotelluric surveys in the Pacific Plate with ages >50 Ma do not show any electrical anomaly that would correspond to the LAB [177,178]. This implies that melt at the LAB is not ubiquitous and would locally explain high electrical values near oceanic ridges [78] and possibly also in the bending lithosphere during the subduction of relatively young plates [179].

As detailed in Section 4, the enhanced plasticity observed in this study is not related to any melting process, consistently with phase diagrams (Figure 2), indicating that the material is far from melting conditions. Instead, TEM observations and EBSD measurements are consistent with solid-state deformation, i.e., GBS and coeval grain rotation (Figure 10). The additional experiments performed on samples with larger grain sizes (Figure 12) exhibit higher values of critical stress, which supports a grain-size sensitive deformation mechanism. The aggregates of nanocrystals resemble shavings planed off larger grains during GBS, which would contribute to the observed plasticity of the germanate samples at 1 atm between 1000 and 1150 °C. For comparison, high-temperature GBS has been evidenced in San Carlos olivine at 300 MPa between 1100 and 1250 °C [111].

Plate lubrication implies lowered viscosities below the lithosphere (e.g., [61,73,75,180]). Low viscosities are favoured by small grain sizes. Comminution, which is significantly enhanced by transformations (e.g., [32,39]), has been evidenced to favour strain localization (e.g., [38,39,181]). The concept of grain-boundary plasticity becomes more and more important in the discussion regarding strain localization processes (e.g., [182]). Superplasticity is associated to diffusion-assisted GBS (e.g., [107,183]) and is documented in

olivine-enstatite aggregates [107,184]. These mantle analogues exhibit mineral aggregation under diffusion-assisted GBS [184] (1200 °C, 270 MPa), as also observed in natural shear zones [185] and in other oxide ceramics (e.g., [183]). In contrast, rheological weakening of olivine-enstatite aggregates was evidenced due to phase mixing in case of dislocation-accommodated GBS [123,124] in the same conditions (1200 °C, 300 MPa). Superplasticity is favoured in case of grain size reduction, enhanced diffusivity, suppressed dynamic grain growth, homogeneous microstructure or reduced number of residual defects [183]. In polyphasic aggregates, Zener pinning often occurs, which drastically limits the grain size (e.g., [186,187]).

Microscopic characteristics of deformation processes induce specific CPO (e.g., [29,107,188]). The changes in CPO observed in the recovered samples (Figure 11) are generally attributed to either H_2O fugacity [36,189], temperature [190,191] or pressure [35,47]. Notably, the temperature-induced activation of the (010)[100] slip system has been reproduced experimentally [55,190], similar to hydrolytic weakening [36]. Olivine slip systems are sensitive to pressure [192] and a pressure-induced slip transition has been evidenced in olivine [35,47]. Grain rotation is likely due to a change of dominant slip system from (010)[100] to (010)[001], as observed in $(Mg_{0.9},Fe_{0.1})_2SiO_4$ between 2.5 GPa and 3.1 GPa, reflecting entrainment of sub-lithospheric mantle in the direction of subduction [35]. These CPO develop in the absence of dislocation activity [191,193] and are consistent with melt-free solid-state deformation [185,191,194]. In addition, such solid-state deformation of peridotite has been associated with a post-seismic slip in natural samples that contain the fossilized trace of a mantle earthquake (>35 km deep) [188,195].

The association of enhanced plasticity and grain rotation suggests that the strength of the boundary between two grains depends on their respective lattice orientations. The structure of olivine grain boundaries is an important question (review by [196]). In particular, natural grain boundaries have their own chemistry because of the incompatibility of some elements within the crystal lattice [196,197]. In addition, highly deformed samples (which reached tertiary creep) show cavitation only in enstatite-free aggregates, whereas enstatite-bearing zones exhibit no cavitation. This suggests that together the olivine and enstatite lattices can form a larger number of compatible grain-to-grain configurations than olivine crystals alone.

Pre-melting, introduced in Section 2, consists of a GB disordering in sub-solidus conditions [41]. This solid-state mechanism provides a robust alternative interpretation for various geophysical signals and has recently been proposed as a possible origin of the asthenosphere [198]. However, as explained above, the temperature window investigated in this study is far from melting or pre-melting conditions, which means that another solid-state phenomenon should be considered.

The unexpected enhanced plasticity evidenced in this study occurs at critical stress values as low as 30 MPa at 1100 °C. According to global dynamics modeling, a basal shear stress as low as only ~10 MPa suffices to allow decoupling from the convecting asthenosphere [71]. If the surprising behavior observed in Mg_2GeO_4 at 1 atm is an equivalent of the deformation mechanism in natural $(Fe,Mg)_2SiO_4$ under LAB conditions, the transient plasticity could account for plate lubrication.

Delayed strain hardening has been observed in $(Fe,Mg)_2SiO_4$ during D-DIA experiments, which is interpreted as a change in dominant slip systems [47] around 3–4 GPa. Low-stress, high-strain experiments on typical dry mantle rock at high pressure and temperature show that at ≈3 GPa, pressure induces the same profound transition in olivine crystallographic preferred orientation as the one produced by high H_2O activity at lower pressure [35]. Above a confining pressure of ≈4 GPa, the gradual hardening of a-slip on (010) over at least a 3–4 GPa pressure interval, rather than a sharp "switch" from one slip system to another, makes meaningless the quest for a single activation volume value for olivine at high pressure [47]. Nevertheless, none of the cited studies unravels the micromechanical phenomenon that could explain the observed switch from enhanced plasticity to

rehardening. It seems unlikely that grain rotation alone could strengthen grain boundaries enough, even though this mechanism cannot be completely ruled out.

5.3. "Asthenosphere" vs. LAB: Collision of Concepts?

Geodetic studies have revealed that for large earthquakes of various magnitudes in different contexts the response of the asthenosphere is similar [199,200]. This suggests that the asthenosphere, regardless of compositional variations and volatiles content, has the intrinsic ability to accommodate tectonic stresses and maintain their basal stress at relatively low values. Indeed, to account for the standard heat flow of 40 mW·m^{-2} at the base of tectonic plates, the viscosity of the asthenosphere should be 3×10^{18} Pa·s [201]. The same estimate of the viscosity is deduced by studies of afterslip relaxation of great earthquakes [74,75], though the methods used are independent. Nevertheless, for both methods the thickness of the low-viscosity asthenospheric layer is the same (~100 km).

Interestingly, different research communities use different definitions of the asthenosphere, which highlights the uncertainties about the nature and distribution of strain beneath tectonic plates. According to geodynamicists, the asthénosphère is the part of the upper mantle in which convection takes place, as illustrated by numerical models (e.g., [71]). In contrast, according to geodesists, the asthenosphere is a layer just below tectonic plates with a low viscosity compared to the average upper mantle (e.g., [73,75,202]). The thickness of the latter is unknown (<200 km; Dr. Luce Fleitout, personal communication) and could actually overlap with the recent LAB concept.

In addition, it is globally observed that the speed of isostatic rebound is comparable to the one of tectonic uplifts, i.e., ~10 mm·year^{-1} [203]. The latter corresponds to the average horizontal velocity of tectonic plates, which suggests that episodic mantle flows within the low-viscosity layer would have the same nature as what controls the steady-state plate velocity.

Assuming a Newtonian fluid for the sake of simplicity, the shear stress τ_s of the low-viscosity layer is related to the viscosity η as follows: $\tau_s = \eta \cdot \dot{\gamma}$, where $\dot{\gamma}$ is the shear strain rate. At the tectonic scale, $\tau_s = \eta \cdot V_{SL}/w$ (Equation (1)) with V_{SL} being the plate velocity ($\sim$1 cm·yr^{-1} = 3×10^{-10} m·s^{-1}) and w the thickness of the low-viscosity layer. Thus, a 200-km-thick layer would correspond to a shear stress of 1.5 kPa whereas a thickness of only 20 km would correspond to a shear stress of 15 kPa. Regarding our experimental results, assuming that $\dot{\gamma} \sim 10^{-5}$·s^{-1}, a viscosity of 3×10^{18} Pa.s would lead (Equation (1)) to a shear stress of 3×10^4 GPa, which is not realistic. To reach realistic values, i.e., $\tau_s \sim 10$ MPa, the viscosity should be $\eta \sim 10^{12}$ Pa·s, as illustrated in Figure 13. This large discrepancy could be explained in two ways: either the LVZ would be much thinner than what we thought (i.e., <100 m instead of >100 km), or the layer would not deform homogeneously but as a population of extremely localized shear zones representing only 0.0001% of its volume considering a 100-km-thick layer (Figure 13), i.e., 0.001% of a 10-km-thick LAB. The trade-off between w and η has been evidenced by geodetic studies on both post-seismic relaxation [74] and post-glacial rebound [204], highlighting the large uncertainty regarding these two interdependent parameters. According to these geodetic studies, a thickness of ~10 km would correspond to a viscosity of $\sim 10^{17}$ Pa·s [74], which would lead to an average shear stress of 3 kPa (Equation (1)). It should also be noted that $\tau_s > 10$ MPa would result in large gravity anomalies, never observed in nature [202,205].

5.4. Open Questions: Implications Regarding Phase Transitions in the Mantle

Considering reaction-induced deformability [40,59,159,206], the impact of transient/unquenchable phases, even in small amounts, could be as important as the one of well-known minerals (e.g., [155,160,171]). As recalled in Section 5.1, the nature, extent and potential implications of phase transformations in the mantle are far from a full understanding and still a matter of ongoing research (e.g., [126,155,171–173]). Softening mechanisms associated with phase transitions of upper mantle minerals have been particularly studied in the scope of earthquakes mechanics (e.g., [28,39]), but part of the results may

also be of significant importance at larger time and space scales. Flattening of the sea-floor depth-age curve has been interpreted as a response to asthenospheric flow [207], and transient changes of the rheology of the asthenosphere due to seasonal variations have been evidenced by geodetic techniques [180]. Transformations, including GB structures, could play a role, at least as important as P-T-dependent rock viscoelasticity, on large-scale deformations induced by mass redistributions at the surface of the Earth [208].

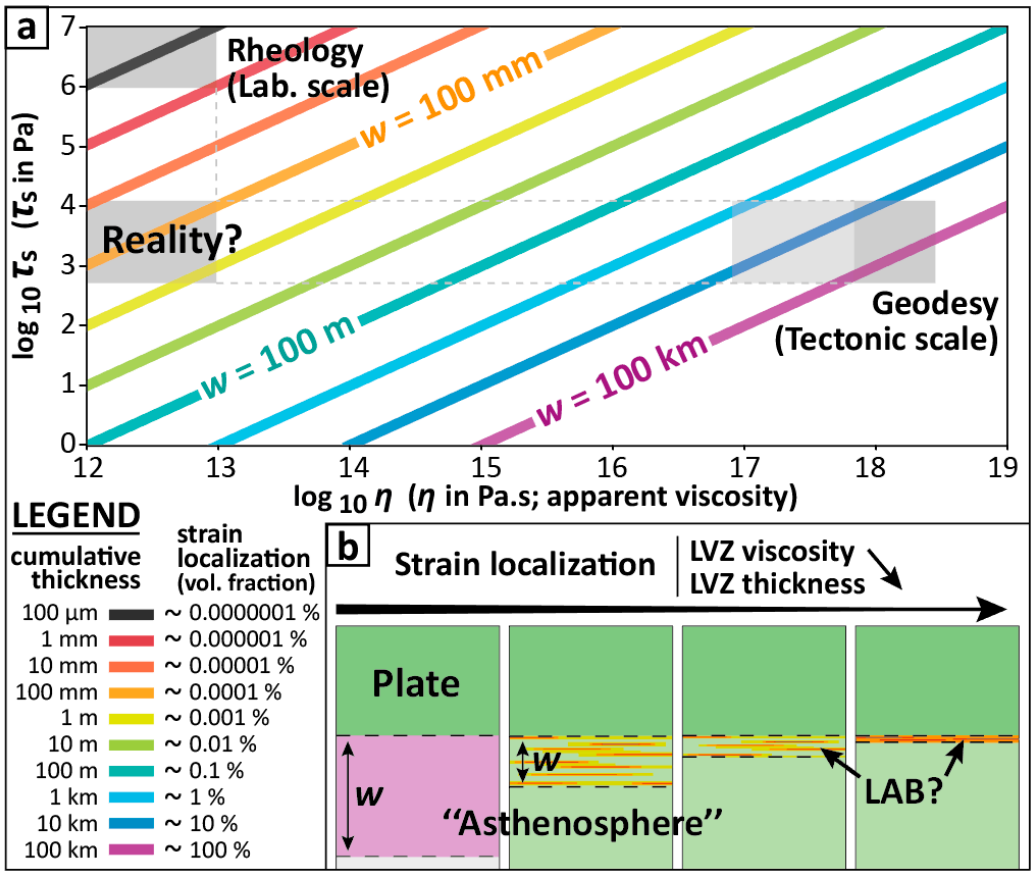

Figure 13. The "asthenosphere" apparent viscosity in question. (**a**) Shear stress at the base of the tectonic plates as a function of the apparent viscosity and thickness (w) of the low-viscosity zone (LVZ) considering the latter as a Newtonian fluid, with comparison between tectonic-scale and laboratory points of view; (**b**) Sketch (not to scale) illustrating the trade-off between the LVZ thickness and its (apparent) viscosity. "Strain localization" accounts for potential inhomogeneous distribution of the decoupling process, and is given in percentages of an arbitrary 100-km-thick asthenosphere.

Additionally, the potential existence of transient ω-olivine in stressed mantle regardless of P-T stability fields could have major consequences on how we understand the solid-state transitions affecting olivine and pyroxenes and related earthquake triggering. At relatively low temperatures (T < 1200 °C, i.e., lithosphere), the ω-olivine is the shear-induced intermediate structure that allows the solid-state transition of olivine to HP spinel phases. Considering our results as exportable to natural olivine at high pressure, we propose that ω-olivine would not form if the mantle remains unstressed ($\sigma < \sigma_c$) at T < 1200 °C. Consequently, the α-olivine would remain metastable, as observed worldwide in cold subducting slabs (e.g., [209,210]).

6. Conclusions

The enhanced plasticity in the MgO-GeO_2 system suggests that some kind of transformation occurs during the deformation of the peridotite analogues in a narrow temperature window. The mechanical data demonstrate that, for 1000 < T < 1150 °C, the derivative of the stress–strain relation of the material drops down to zero once a critical stress as low as

30–100 MPa is reached. The enhanced plasticity is followed by a sharp hardening, similarly to what is commonly observed in steels during the shear-induced transformation from austenite to martensite, the final material being significantly harder. This TRansformation-Induced Plasticity, widely observed in TRIP alloys, is evidenced here for the first time in this mantle analogue.

The high-temperature solid-state deformation is confirmed and would operate via "transformation"-assisted grain-boundary sliding, possibly due to the stress-induced formation of a transient metastable phase or grain-boundary disorganization that would occur at temperatures between 1000 and 1150 °C. The transient metastable phase could be the ω-olivine, which stability field in a P-T-σ diagram is unknown and may not even exist. Another possibility is the transition from orthoenstatite to protoenstatite or *Cmca*-enstatite, which stability is debated. The "transformation" appears to occur at grain boundaries, as coeval grain rotation and grain boundary sliding of olivine are likely. The EBSD mapping would be consistent with accommodation on the (010)[100] slip system. No dislocation is observed. The absence of amorphization at grain boundaries is also documented. The transition seems to occur as a result of a competition between diffusional and displacive processes, i.e., temperature vs. strain rate, making the material harder at 1200 °C than at 1100 °C thanks to diffusion that would stabilize thermodynamically stable phases.

The enhanced plasticity evidenced in the MgO-GeO_2 system brings into light an alternative scenario to explain the LAB, which does not require H_2O. Contrary to what is commonly assumed, partial melting is not the only process that may explain the LAB, and might not be required at all. If partial melting were responsible for decoupling at the LAB, enormous amounts of volatiles would be required to allow the actual plate motion. Here we show that this lubrication could be due to another process. The nature of the "transformation" that seems to affect the vicinity of grain boundaries, still needs to be deciphered, but our results demonstrate that the viscosity reduction has nothing to do with partial melting. In addition, the presence of volatiles at the LAB would necessarily lead to significantly higher diffusivity, either intracrystalline or at grain boundaries, which is not inconsistent with our findings.

The critical stress values reported in our study seem compatible with modeling of global geodynamics, but further investigations are required to understand how representative our experiments are for tectonic-scale considerations. Experimental works are needed to better understand the potential role of stress-induced transient stability of phases that would be considered as "metastable". We suggest that such phase might transiently form during the superplastic process, which is likely to consist of a general grain-boundary disordering similar to pre-melting. Hence, we question whether phase or grain boundary stability and reaction-induced deformability are underestimated in our understanding of the upper mantle. We insist to the Earth Sciences community on the need to look at grain boundaries as phases that have their own domain of stability.

In light of these results, HP-HT experiments should be designed to check in which conditions such plasticity occurs in the MgO-FeO-SiO_2 system. This may constitute the birth of a new paradigm: tectonic plates may slide on a layer in which the peridotite is constantly adjusting via a process resembling "cold welding". For relatively old plates (~50 Ma or older), the LAB might not result from partial melting or volatiles gathering, but from a solid-state disordering.

Supplementary Materials: The following are available online at https://www.mdpi.com/article/10.3390/min11060600/s1: Figure S1: Record of parameters during spark plasma sintering; Figure S2: Raman spectroscopy and X-ray diffraction (XRD) analyses; Figure S3: Additional SEM images for SP-307 (Material representative of the material used for the systematic experimental protocol); Figure S4: SEM imaging of SP-308 (Material not selected for the systematic experimental protocol); Figure S5: Detailed view of Figure 5b; Table S1: Results of the calcination step; Table S2: Results of the spark plasma sintering step; Table S3: Summary of deformation conditions; Table S4: Data acquisition conditions for EBSD measurements.

Author Contributions: This study is the result of the TROPICO project (TRansforming Olivine: Plasticity and Induced Crystallographic Orientation) drawn up in 2017 and implemented in 2018 by T.P.F., who performed the synthesis, deformation experiments, SEM imaging and X-ray diffraction. D.D. performed the TEM imaging and EBSD analysis. T.P.F. processed the data, set the context, proposed interpretations in light of the literature and wrote the paper. Both authors have read and agreed to the published version of the manuscript.

Funding: This research was funded by the International Research Promotion Office of the Earthquake Research Institute, TROPICO project (TPF's grant).

Data Availability Statement: The processed mechanical data and associated imaging and analyses are presented and described in this study and supplementary information. The raw mechanical data are available upon request from the corresponding author.

Acknowledgments: T.P.F. thanks Takehiko Hiraga for hosting him in the Earth Material Science team for the TROPICO project in 2018. We thank Sanae Koizumi and Atsuro Okamoto for their kind explanations about SPS sintering, the 1-atm rig and previous experimental achievements. We thank Hatsuki Yamauchi, Luce Fleitout, Bruno Reynard and Kenji Mibe for key discussions. Finally, we thank Pamela Burnley for proposing to challenge the results with additional samples from previous studies. This paper has benefited from deep criticism from a total of six anonymous reviewers before and after submission to the journal.

Conflicts of Interest: The authors declare no conflict of interest. The funders had no role in the design of the study; in the collection, analyses, or interpretation of data; in the writing of the manuscript, or in the decision to publish the results.

References

1. Valencia, D.; O'Connell, R.J.; Sasselov, D.D. Inevitability of plate tectonics on super-Earths. *Astrophys. J. Lett.* **2007**, *670*, L45. [CrossRef]
2. Valentine, J.W.; Moores, E.M. Plate tectonics and the history of life in the oceans. *Sci. Am.* **1974**, *230*, 80–89. [CrossRef]
3. Parnell, J. Plate tectonics, surface mineralogy, and the early evolution of life. *Int. J. Astrobiol.* **2004**, *3*, 131–137. [CrossRef]
4. Santosh, M. A synopsis of recent conceptual models on supercontinent tectonics in relation to mantle dynamics, life evolution and surface environment. *J. Geodyn.* **2010**, *50*, 116–133. [CrossRef]
5. Wegener, A.A. *The Origin of Continents and Oceans*; Courier Dover Publications: Mineola, NY, USA, 2011; ISBN 978-0-486-61708-4.
6. Lliboutry, L. Sea-floor spreading, continental drift and lithosphere sinking with an asthenosphere at melting point. *J. Geophys. Res. Space Phys.* **1969**, *74*, 6525–6540. [CrossRef]
7. McKenzie, D.P. Plate tectonics of the Mediterranean region. *Nature* **1970**, *226*, 239–243. [CrossRef]
8. Vogt, P. Asthenosphere motion recorded by the ocean floor south of Iceland. *Earth Planet. Sci. Lett.* **1971**, *13*, 153–160. [CrossRef]
9. Froidevaux, C.; Schubert, G. Plate motion and structure of the continental asthenosphere: A realistic model of the upper mantle. *J. Geophys. Res. Space Phys.* **1975**, *80*, 2553–2564. [CrossRef]
10. Barrell, J. The strength of the Earth's crust. *J. Geol.* **1914**, *22*, 655–683. [CrossRef]
11. Barrell, J. The Strength of the Earth's Crust VIII. Physical Conditions Controlling the Nature of Lithosphere and Asthenosphere. *J. Geol.* **1915**, *23*, 425–443. [CrossRef]
12. Holmes, A. A review of the continental drift hypothesis. *Min. Publ.* **1929**, 1–15.
13. Rychert, C.A.; Fischer, K.M.; Rondenay, S. A sharp lithosphere-asthenosphere boundary imaged beneath eastern North America. *Nature* **2005**, *436*, 542. [CrossRef] [PubMed]
14. Green, D.H.; Hibberson, W.O.; Kovács, I.; Rosenthal, A. Water and its influence on the lithosphere-asthenosphere boundary. *Nature* **2010**, *467*, 448–451. [CrossRef]
15. Schmerr, N. The Gutenberg discontinuity: Melt at the lithosphere-asthenosphere boundary. *Science* **2012**, *335*, 1480–1483. [CrossRef]
16. Naif, S.; Key, K.; Constable, S.; Evans, R.L. Melt-rich channel observed at the lithosphere-asthenosphere boundary. *Nature* **2013**, *495*, 356–359. [CrossRef] [PubMed]
17. Yamauchi, H.; Takei, Y. Application of a Premelting Model to the Lithosphere-Asthenosphere Boundary. *Geochem. Geophys. Geosyst.* **2020**, *21*, e2020GC009338. [CrossRef]
18. Conrad, C.P.; Lithgow-Bertelloni, C. How mantle slabs drive plate tectonics. *Science* **2002**, *298*, 207–209. [CrossRef] [PubMed]
19. Mallard, C.; Coltice, N.; Seton, M.; Müller, R.D.; Tackley, P.J. Subduction controls the distribution and fragmentation of Earth's tectonic plates. *Nature* **2016**, *535*, 140–143. [CrossRef]
20. Leven, J.H.; Jackson, I.; Ringwood, A.E. Upper mantle seismic anisotropy and lithospheric decoupling. *Nature* **1981**, *289*, 234. [CrossRef]
21. Furukawa, Y. Depth of the decoupling plate interface and thermal structure under arcs. *J. Geophys. Res. Solid Earth* **1993**, *98*, 20005–20013. [CrossRef]

22. Hirth, G.; Kohlstedt, D.L. Water in the oceanic upper mantle: Implications for rheology, melt extraction and the evolution of the lithosphere. *Earth Planet. Sci. Lett.* **1996**, *144*, 93–108. [CrossRef]
23. Stern, T.A.; Henrys, S.A.; Okaya, D.; Louie, J.N.; Savage, M.K.; Lamb, S.; Sato, H.; Sutherland, T.; Iwasaki, T. A seismic reflection image for the base of a tectonic plate. *Nature* **2015**, *518*, 85. [CrossRef]
24. Kita, S.; Ferrand, T.P. Physical mechanisms of oceanic mantle earthquakes: Comparison of natural and experimental events. *Sci. Rep.* **2018**, *8*, 17049. [CrossRef] [PubMed]
25. Carter, N.L.; Tsenn, M.C. Flow properties of continental lithosphere. *Tectonophysics* **1987**, *136*, 27–63. [CrossRef]
26. Cannat, M. How thick is the magmatic crust at slow spreading oceanic ridges? *J. Geophys. Res. Solid Earth* **1996**, *101*, 2847–2857. [CrossRef]
27. Cannat, M.; Fontaine, F.; Escartin, J. Serpentinization and associated hydrogen and methane fluxes at slow spreading ridges. In *Diversity* of Hydrothermal Systems on Slow Spreading Ocean Ridges; AGU: Washington, DC, USA, 2010; Volume 188, pp. 241–264.
28. Kirby, S.H. Rheology of the lithosphere. *Rev. Geophys.* **1983**, *21*, 1458–1487. [CrossRef]
29. Hansen, L.N.; Zimmerman, M.E.; Kohlstedt, D.L. Laboratory measurements of viscous anisotropy of olivine aggregates. *Nature* **2013**, *492*, 415–418. [CrossRef]
30. Nakakoji, T.; Hiraga, T.; Nagao, H.; Ito, S.; Kano, M. Diffusion creep and grain growth in forsterite +20 vol% enstatite aggregates: 1. High-resolution experiments and their data analyses. *J. Geophys. Res. Solid Earth* **2018**, *123*, 9486–9512. [CrossRef]
31. Nakakoji, T.; Hiraga, T. Diffusion creep and grain growth in forsterite +20 vol% enstatite aggregates: 2. Their common diffusional mechanism and its consequence for weak-temperature-dependent viscosity. *J. Geophys. Res. Solid Earth* **2018**, *123*, 9513–9527. [CrossRef]
32. Ferrand, T.P. Seismicity and mineral destabilizations in the subducting mantle up to 6 GPa, 200 km depth. *Lithos* **2019**, *334*, 205–230. [CrossRef]
33. Karato, S.I. Does partial melting reduce the creep strength of the upper mantle? *Nature* **1986**, *319*, 309. [CrossRef]
34. Karato, S.I. On the origin of the asthenosphere. *Earth Planet. Sci. Lett.* **2012**, *321*, 95–103. [CrossRef]
35. Jung, H.; Mo, W.; Green, H.W. Upper mantle seismic anisotropy resulting from pressure-induced slip transition in olivine. *Nat. Geosci.* **2009**, *2*, 73. [CrossRef]
36. Girard, J.; Chen, J.; Raterron, P.; Holyoke, C.W. Hydrolytic weakening of olivine at mantle pressure: Evidence of [100] slip system softening from single-crystal deformation experiments. *Phys. Earth Planet. Inter.* **2013**, *216*, 12–20. [CrossRef]
37. Warren, J.M.; Hirth, G. Grain size sensitive deformation mechanisms in naturally deformed peridotites. *Earth Planet. Sci. Lett.* **2006**, *248*, 438–450. [CrossRef]
38. Thielmann, M. Grain size assisted thermal runaway as a nucleation mechanism for continental mantle earthquakes: Impact of complex rheologies. *Tectonophysics* **2018**, *746*, 611–623. [CrossRef]
39. Green, H.W., II; Shi, F.; Bozhilov, K.; Xia, G.; Reches, A.Z. Phase transformation and nanometric flow cause extreme weakening during fault slip. *Nat. Geosci.* **2015**, *8*, 484. [CrossRef]
40. Wheeler, J. A unifying basis for the interplay of stress and chemical processes in the Earth: Support from diverse experiments. *Contrib. Mineral. Petrol.* **2020**, *175*, 1–27. [CrossRef]
41. Yamauchi, H.; Takei, Y. Polycrystal anelasticity at near-solidus temperatures. *J. Geophys. Res. Solid Earth* **2016**, *121*, 7790–7820. [CrossRef]
42. Takei, Y. Grain Boundary Disordering Just Before Partial Melting. In Proceedings of the AGU Fall Meeting Abstracts, New Orleans, LA, USA, 12 December 2017.
43. Griggs, D. Hydrolytic weakening of quartz and other silicates. *Geophys. J. Int.* **1967**, *14*, 19–31. [CrossRef]
44. Précigout, J.; Stünitz, H.; Pinquier, Y.; Champallier, R.; Schubnel, A. High-pressure, High-temperature Deformation Experiment Using the New Generation Griggs-type Apparatus. *JoVE J. Vis. Exp.* **2018**, *134*, e56841. [CrossRef]
45. Schubnel, A.; Brunet, F.; Hilairet, N.; Gasc, J.; Wang, Y.; Green, H.W. Deep-focus earthquake analogs recorded at high pressure and temperature in the laboratory. *Science* **2013**, *341*, 1377–1380. [CrossRef]
46. Ferrand, T.P.; Hilairet, N.; Incel, S.; Deldicque, D.; Labrousse, L.; Gasc, J.; Renner, J.; Wang, Y.; Green, H.W., II; Schubnel, A. Dehydration-driven stress transfer triggers intermediate-depth earthquakes. *Nat. Commun.* **2017**, *8*, 15247. [CrossRef] [PubMed]
47. Hilairet, N.; Wang, Y.; Sanehira, T.; Merkel, S.; Mei, S. Deformation of olivine under mantle conditions: An in situ high-pressure, high-temperature study using monochromatic synchrotron radiation. *J. Geophys. Res. Solid Earth* **2012**, *117*. [CrossRef]
48. Ozima, M.; Akimoto, S.I. Flux growth of single crystals of $MgGeO_3$ polymorphs (orthopyroxene, clinopyroxene, and ilmenite) and their phase relations and crystal structures. *Am. Mineral.* **1983**, *68*, 1199–1205.
49. Jackson, J.M.; Sinogeikin, S.V.; Carpenter, M.A.; Bass, J.D. Novel phase transition in orthoenstatite. *Am. Mineral.* **2004**, *89*, 239–244. [CrossRef]
50. Ringwood, A.E. The system Mg_2SiO_4–Mg_2GeO_4. *Am. J. Sci.* **1956**, *254*, 707–711. [CrossRef]
51. Dachille, F.; Roy, R. System Mg_2SiO_4–Mg_2GeO_4 at 10,000, 60,000 and about 300,000 psi. *Bull. Geol. Soc. Am.* **1956**, *67*, 1682.
52. Robbins, C.R.; Levin, E.M. The system magnesium oxide-germanium dioxide. *Am. J. Sci.* **1959**, *257*, 63–70. [CrossRef]
53. Shiota, K.; Miyamoto, Y.; Takubo, H.; Koizumi, M. Phase Stability of Mg_2GeO_4 Under Pressures. In Proceedings of the 8th AIRAPT Conference, Uppsala, Sweden, 17–22 August 1981; pp. 744–750.
54. Ross, N.L.; Navrotsky, A. Study of the $MgGeO_3$ polymorphs (orthopyroxene, clinopyroxene, and ilmenite structures) by calorimetry, spectroscopy, and phase equilibria. *Am. Mineral.* **1988**, *73*, 1355–1365.

55. Dupas-Bruzek, C.; Tingle, T.N.; Green, H.W., II; Doukhan, N.; Doukhan, J.C. The rheology of olivine and spinel magnesium germanate (Mg_2GeO_4): TEM study of the defect microstructures. *Phys. Chem. Miner.* **1998**, *25*, 501–514. [CrossRef]
56. Mecklenburgh, J.; Zhao, Y.H.; Heidelbach, F.; Mackwell, S. Deformation of olivine-spinel aggregates in the system $(Mg,Ni)_2GeO_4$ deformed to high strain in torsion: Implications for upper mantle anisotropy. *J. Geophys. Res. Solid Earth* **2006**, *111*. [CrossRef]
57. Shi, F.; Zhang, J.; Xia, G.; Jin, Z.; Green, H.W. Rheology of Mg_2GeO_4 olivine and spinel harzburgite: Implications for Earth's mantle transition zone. *Geophys. Res. Lett.* **2015**, *42*, 2212–2218. [CrossRef]
58. Green, H.W.; Burnley, P.C. A new self-organizing mechanism for deep-focus earthquakes. *Nature* **1989**, *341*, 733. [CrossRef]
59. Officer, T.; Secco, R.A. Detection of high P, T transformational faulting in Fe_2SiO_4 via in-situ acoustic emission: Relevance to deep-focus earthquakes. *Phys. Earth Planet. Inter.* **2020**, *300*, 106429. [CrossRef]
60. Fei, Y.; Bertka, C.M. Phase transitions in the Earth's mantle and mantle mineralogy. In *Mantle Petrology: Field Observations & High-Pressure Experimentation*; Oxford University Press: Oxford, UK, 1999; Volume 6, pp. 189–207.
61. Kumar, P.; Kind, R.; Hanka, W.; Wylegalla, K.R.C.H.; Reigber, C.; Yuan, X.; Woelbern, I.; Schwintzer, P.; Fleming, K.; Larsen, T.B. The lithosphere-asthenosphere boundary in the North-West Atlantic region. *Earth Planet. Sci. Lett.* **2005**, *236*, 249–257. [CrossRef]
62. Kawakatsu, H.; Kumar, P.; Takei, Y.; Shinohara, M.; Kanazawa, T.; Araki, E.; Suyehiro, K. Seismic evidence for sharp lithosphere-asthenosphere boundaries of oceanic plates. *Science* **2009**, *324*, 499–502. [CrossRef] [PubMed]
63. Fischer, K.M.; Ford, H.A.; Abt, D.L.; Rychert, C.A. The lithosphere-asthenosphere boundary. *Annu. Rev. Earth Planet. Sci.* **2010**, *38*, 551–575. [CrossRef]
64. Doglioni, C.; Ismail-Zadeh, A.; Panza, G.; Riguzzi, F. Lithosphere–asthenosphere viscosity contrast and decoupling. *Phys. Earth Planet. Inter.* **2011**, *189*, 1–8. [CrossRef]
65. Gaetani, G.A.; Grove, T.L. The influence of water on melting of mantle peridotite. *Contrib. Mineral. Petrol.* **1998**, *131*, 323–346. [CrossRef]
66. Hirschmann, M.M.; Tenner, T.; Aubaud, C.; Withers, A.C. Dehydration melting of nominally anhydrous mantle: The primacy of partitioning. *Phys. Earth Planet. Inter.* **2009**, *176*, 54–68. [CrossRef]
67. Sarafian, E.; Gaetani, G.A.; Hauri, E.H.; Sarafian, A.R. Experimental constraints on the damp peridotite solidus and oceanic mantle potential temperature. *Science* **2017**, *355*, 942–945. [CrossRef] [PubMed]
68. Burke, K. Plate tectonics, the Wilson Cycle, and mantle plumes: Geodynamics from the top. *Annu. Rev. Earth Planet. Sci.* **2011**, *39*, 1–29. [CrossRef]
69. Le Pichon, X.; Francheteau, J.; Bonnin, J. *Plate Tectonics*; Elsevier: Amsterdam, The Netherlands, 2013; Volume 6.
70. Savage, J.C.; Prescott, W.H. Asthenosphere readjustment and the earthquake cycle. *J. Geophys. Res. Solid Earth* **1978**, *83*, 3369–3376. [CrossRef]
71. Coltice, N.; Gérault, M.; Ulvrová, M. A mantle convection perspective on global tectonics. *Earth Sci. Rev.* **2017**, *165*, 120–150. [CrossRef]
72. Becker, T.W.; Conrad, C.P.; Schaeffer, A.J.; Lebedev, S. Origin of azimuthal seismic anisotropy in oceanic plates and mantle. *Earth Planet. Sci. Lett.* **2014**, *401*, 236–250. [CrossRef]
73. Becker, T.W. Superweak asthenosphere in light of upper mantle seismic anisotropy. *Geochem. Geophys. Geosyst.* **2017**, *18*, 1986–2003. [CrossRef]
74. Hu, Y.; Bürgmann, R.; Banerjee, P.; Feng, L.; Hill, E.M.; Ito, T.; Tabei, T.; Wang, K. Asthenosphere rheology inferred from observations of the 2012 Indian Ocean earthquake. *Nature* **2016**, *538*, 368–372. [CrossRef]
75. Klein, E.; Fleitout, L.; Vigny, C.; Garaud, J.D. Afterslip and viscoelastic relaxation model inferred from the large-scale post-seismic deformation following the 2010 M w 8.8 Maule earthquake (Chile). *Geophys. J. Int.* **2016**, *205*, 1455–1472. [CrossRef]
76. Ross, N.L.; Navrotsky, A. The Mg_2GeO_4 olivine-spinel phase transition. *Phys. Chem. Mineral.* **1987**, *14*, 473–481. [CrossRef]
77. Holtzman, B.K.; Kendall, J.M. Organized melt, seismic anisotropy, and plate boundary lubrication. *Geochem. Geophys. Geosyst.* **2010**, *11*. [CrossRef]
78. Evans, R.L.; Hirth, G.; Baba, K.; Forsyth, D.; Chave, A.; Mackie, R. Geophysical evidence from the MELT area for compositional controls on oceanic plates. *Nature* **2005**, *437*, 249–252. [CrossRef]
79. Baba, K.; Chave, A.D.; Evans, R.L.; Hirth, G.; Mackie, R.L. Mantle dynamics beneath the East Pacific Rise at 17 S: Insights from the Mantle Electromagnetic and Tomography (MELT) experiment. *J. Geophys. Res. Solid Earth* **2006**, *111*. [CrossRef]
80. Yoshino, T.; Shimojuku, A.; Shan, S.; Guo, X.; Yamazaki, D.; Ito, E.; Higo, Y.; Funakoshi, K.I. Effect of temperature, pressure and iron content on the electrical conductivity of olivine and its high-pressure polymorphs. *J. Geophys. Res.* **2012**, *117*. [CrossRef]
81. Gaillard, F.; Malki, M.; Iacono-Marziano, G.; Pichavant, M.; Scaillet, B. Carbonatite melts and electrical conductivity in the asthenosphere. *Science* **2008**, *322*, 1363–1365. [CrossRef] [PubMed]
82. Caricchi, L.; Gaillard, F.; Mecklenburgh, J.; Le Trong, E. Experimental determination of electrical conductivity during deformation of melt-bearing olivine aggregates: Implications for electrical anisotropy in the oceanic low velocity zone. *Earth Planet. Sci. Lett.* **2011**, *302*, 81–94. [CrossRef]
83. Sifré, D.; Gardés, E.; Massuyeau, M.; Hashim, L.; Hier-Majumder, S.; Gaillard, F. Electrical conductivity during incipient melting in the oceanic low-velocity zone. *Nature* **2014**, *509*, 81. [CrossRef]
84. Roberts, J.J.; Tyburczy, J.A. Partial-melt electrical conductivity: Influence of melt composition. *J. Geophys. Res. Solid Earth* **1999**, *104*, 7055–7065. [CrossRef]
85. Evans, R.L. Carbon in Charge. *Science* **2008**, *322*, 1338–1340. [CrossRef] [PubMed]

86. Turcotte, D.L.; Schubert, G. *Geodynamics*; Cambridge University Press: Cambridge, UK, 2002.
87. Holtzman, B.K.; Groebner, N.J.; Zimmerman, M.E.; Ginsberg, S.B.; Kohlstedt, D.L. Stress-driven melt segregation in partially molten rocks. *Geochem. Geophys. Geosyst.* **2003**, *4*. [CrossRef]
88. Takei, Y.; Holtzman, B.K. Viscous constitutive relations of solid-liquid composites in terms of grain boundary contiguity: 3. Causes and consequences of viscous anisotropy. *J. Geophys. Res. Solid Earth* **2009**, *114*. [CrossRef]
89. Zhang, B.; Yoshino, T.; Yamazaki, D.; Manthilake, G.; Katsura, T. Electrical conductivity anisotropy in partially molten peridotite under shear deformation. *Earth Planet. Sci. Lett.* **2014**, *405*, 98–109. [CrossRef]
90. Ferrand, T.P. Conductive channels in the deep oceanic lithosphere could consist of garnet pyroxenites at the fossilized lithosphere–asthenosphere boundary. *Minerals* **2020**, *10*, 1107. [CrossRef]
91. Ten Grotenhuis, S.M.; Drury, M.R.; Peach, C.J.; Spiers, C.J. Electrical properties of fine-grained olivine: Evidence for grain boundary transport. *J. Geophys. Res. Solid Earth* **2004**, *109*. [CrossRef]
92. Karato, S.I. The role of hydrogen in the electrical conductivity of the upper mantle. *Nature* **1990**, *347*, 272. [CrossRef]
93. Akimoto, S.I.; Fujisawa, H. Demonstration of the electrical conductivity jump produced by the olivine-spinel transition. *J. Geophys. Res.* **1965**, *70*, 443–449. [CrossRef]
94. Incel, S.; Hilairet, N.; Labrousse, L.; John, T.; Deldicque, D.; Ferrand, T.; Wang, Y.; Renner, J.; Morales, R.; Schubnel, A. Laboratory earthquakes triggered during eclogitization of lawsonite-bearing blueschist. *Earth Planet. Sci. Lett.* **2017**, *459*, 320–331. [CrossRef]
95. Ferrand, T.P. Garnet pyroxenites explain high electrical conductivity in the East African deep lithosphere. *Nat. Geosci.* **2021**, submitted.
96. Hirschmann, M.M. Water, melting, and the deep Earth H_2O cycle. *Annu. Rev. Earth Planet. Sci.* **2006**, *34*, 629–653. [CrossRef]
97. Schmidt, M.W.; Poli, S. Experimentally based water budgets for dehydrating slabs and consequences for arc magma generation. *Earth Planet. Sci. Lett.* **1998**, *163*, 361–379. [CrossRef]
98. John, T.; Gussone, N.; Podladchikov, Y.Y.; Bebout, G.E.; Dohmen, R.; Halama, R.; Klemd, R.; Magna, T.; Seitz, H.M. Volcanic arcs fed by rapid pulsed fluid flow through subducting slabs. *Nat. Geosci.* **2012**, *5*, 489. [CrossRef]
99. McBirney, A.R. Oceanic volcanism: A review. *Rev. Geophys.* **1971**, *9*, 523–556. [CrossRef]
100. Hirth, G.; Kohlstedt, D.L. The stress dependence of olivine creep rate: Implications for extrapolation of lab data and interpretation of recrystallized grain size. *Earth Planet. Sci. Lett.* **2015**, *418*, 20–26. [CrossRef]
101. Bollinger, C.; Merkel, S.; Raterron, P.; Cordier, P. Olivine dislocation creep: Revisiting experimental data to 8 GPa pressure. *Phys. Earth Planet. Inter.* **2013**, *228*, 211–219. [CrossRef]
102. Kohlstedt, D.L. The role of water in high-temperature rock deformation. *Rev. Mineral. Geochem.* **2006**, *62*, 377–396. [CrossRef]
103. Hirth, G.; Kohlstedt, D.L. Experimental constraints on the dynamics of partially molten upper mantle 2: Deformation in the dislocation creep regime. *J. Geophys. Res.* **1995**, *100*, 15441–15449. [CrossRef]
104. Frost, H.J.; Ashby, M.F. *Deformation Mechanism Maps: The Plasticity and Creep of Metals and Ceramics*; Pergamon Press: Oxford, UK, 1982.
105. Raterron, P.; Bollinger, C.; Merkel, S. Olivine intergranular plasticity at mantle pressures and temperatures. *C. R. Geosci.* **2019**, *351*, 80–85. [CrossRef]
106. Coble, R.L. A model for boundary diffusion-controlled creep in polycrystalline materials. *J. Appl. Phys.* **1963**, *34*, 1679–1682. [CrossRef]
107. Hiraga, T.; Miyazaki, T.; Tasaka, M.; Yoshida, H. Mantle superplasticity and its self-made demise. *Nature* **2010**, *468*, 1091. [CrossRef] [PubMed]
108. Ashby, M.F. On interface-reaction control of Nabarro-Herring creep and sintering. *Scr. Metall.* **1969**, *3*, 837–842. [CrossRef]
109. Goldsby, D.L. Superplastic flow of ice relevant to glacier and ice-sheet mechanics. In *Glacier Science & Environmental Change*; Blackwell Science Ltd.: Hoboken, NJ, USA, 2006; pp. 308–314.
110. Ghosh, S.; Koizumi, S.; Hiraga, K. Diffusion creep of diopside. *J. Geophys. Res. Solid Earth* **2021**, *126*. [CrossRef]
111. Hansen, L.N.; Zimmerman, M.E.; Kohlstedt, D.L. Grain boundary sliding in San Carlos olivine: Flow law parameters and crystallographic-preferred orientation. *J. Geophys. Res. Solid Earth* **2011**, *116*. [CrossRef]
112. Hirth, G.; Kohlstedt, D.L. Rheology of the upper mantle and the mantle wedge: A view from the experimentalists. *Geophys. Monogr. Am. Geophys. Union* **2003**, *138*, 83–106.
113. Ohuchi, T.; Kawazoe, T.; Higo, Y.; Funakoshi, K.I.; Suzuki, A.; Kikegawa, T.; Irifune, T. Dislocation-accommodated grain boundary sliding as the major deformation mechanism of olivine in the Earth's upper mantle. *Sci. Adv.* **2015**, *1*, e1500360. [CrossRef]
114. Cordier, P.; Demouchy, S.; Beausir, B.; Taupin, V.; Barou, F.; Fressengeas, C. Disclinations provide the missing mechanism for deforming olivine-rich rocks in the mantle. *Nature* **2014**, *504*, 51–56. [CrossRef]
115. Castelnau, O.; Blackman, D.K.; Lebensohn, R.A.; Ponte Castañeda, P. Micromechanical modeling of the viscoplastic behavior of olivine. *J. Geophys. Res. Solid Earth* **2008**, *113*. [CrossRef]
116. Tordesillas, A.; Zhang, J.; Behringer, R. Buckling force chains in dense granular assemblies: Physical and numerical experiments. *Geomech. Geoeng. Int. J.* **2009**, *4*, 3–16. [CrossRef]
117. Burnley, P.C. The importance of stress percolation patterns in rocks and other polycrystalline materials. *Nat. Commun.* **2013**, *4*, 2117. [CrossRef]
118. Tielke, J.A.; Hansen, L.N.; Tasaka, M.; Meyers, C.; Zimmerman, M.E.; Kohlstedt, D.L. Observations of grain size sensitive power law creep of olivine aggregates over a large range of lattice-preferred orientation strength. *J. Geophys. Res. Solid Earth* **2016**, *121*, 506–516. [CrossRef]

119. Avé Lallemant, H.G. Experimental deformation of diopside and websterite. *Tectonophysics* **1978**, *48*, 1–27. [CrossRef]
120. Skrotzki, W. Defect structure and deformation mechanisms in naturally deformed augite and enstatite. *Tectonophysics* **1994**, *229*, 43–68. [CrossRef]
121. Kirby, S.H.; Kronenberg, A.K. Deformation of clinopyroxenite: Evidence for a transition in flow mechanisms and semibrittle behavior. *J. Geophys. Res. Solid Earth* **1984**, *89*, 3177–3192. [CrossRef]
122. Hansen, L.N.; Warren, J.M. Quantifying the effect of pyroxene on deformation of peridotite in a natural shear zone. *J. Geophys. Res. Solid Earth* **2015**, *120*, 2717–2738. [CrossRef]
123. Tasaka, M.; Zimmerman, M.E.; Kohlstedt, D.L. Rheological weakening of olivine+ orthopyroxene aggregates due to phase mixing: Part 1. Mechanical behavior. *J. Geophys. Res. Solid Earth* **2017**, *122*, 7584–7596. [CrossRef]
124. Tasaka, M.; Zimmerman, M.E.; Kohlstedt, D.L.; Stünitz, H.; Heilbronner, R. Rheological weakening of olivine + orthopyroxene aggregates due to phase mixing: Part 2. Microstructural development. *J. Geophys. Res. Solid Earth* **2017**, *122*, 7597–7612. [CrossRef]
125. Koizumi, S.; Hiraga, T.; Tachibana, C.; Tasaka, M.; Miyazaki, T.; Kobayashi, T.; Asako, T.; Naoki, O.; Sano, S. Synthesis of highly dense and fine-grained aggregates of mantle composites by vacuum sintering of nano-sized mineral powders. *Phys. Chem. Mineral.* **2010**, *37*, 505–518. [CrossRef]
126. Tomioka, N.; Okuchi, T. A new high-pressure form of Mg_2SiO_4 highlighting diffusionless phase transitions of olivine. *Sci. Rep.* **2017**, *7*, 17351. [CrossRef] [PubMed]
127. Navrotsky, A. Synthesis of Mg_2GeO_4 from Tetraethylorthogermanate. *J. Am. Ceram. Soc.* **1970**, *53*, 696. [CrossRef]
128. Hamilton, D.T.; Henderson, C.M.B. The preparation of silicate compositions by a gelling method. *Mineral. Mag. J. Mineral. Soc.* **1968**, *36*, 832–838. [CrossRef]
129. Koizumi, S.; Hiraga, T.; Suzuki, T.S. Vickers indentation tests on olivine: Size effects. *Phys. Chem. Mineral.* **2020**, *47*, 8. [CrossRef]
130. Kirfel, A.; Neuhaus, A. Zustandsverhalten und elektrische Leitfähigkeit von $MgGeO_3$ bei Drücken bis 65 kbar und Temperaturen bis 1300 °C (mit Folgerungen für das Druckverhalten von $MgSiO_3$). *Z. Phys. Chem.* **1974**, *91*, 121–152. [CrossRef]
131. Burnley, P.C.; Green, H.W.; Prior, D.J. Faulting associated with the olivine to spinel transformation in Mg_2GeO_4 and its implications for deep-focus earthquakes. *J. Geophys. Res. Solid Earth* **1991**, *96*, 425–443. [CrossRef]
132. Riggs, E.M.; Green, H.W. A new class of microstructures which lead to transformation-induced faulting in magnesium germanate. *J. Geophys. Res. Solid Earth* **2005**, *110*. [CrossRef]
133. Wyatt, O.H. Transient creep in pure metals. *Phys. Soc. Sect. B* **1953**, *66*, 459. [CrossRef]
134. Eucken, S.; Duerig, T.W. The effects of pseudoelastic prestraining on the tensile behaviour and two-way shape memory effect in aged NiTi. *Acta Metall.* **1989**, *37*, 2245–2252. [CrossRef]
135. Lagoudas, D.C.; Entchev, P.B. Modeling of transformation-induced plasticity and its effect on the behavior of porous shape memory alloys. Part I: Constitutive model for fully dense SMAs. *Mech. Mater.* **2004**, *36*, 865–892. [CrossRef]
136. Heller, L.; Seiner, H.; Šittner, P.; Sedlák, P.; Tyc, O.; Kadeřávek, L. On the plastic deformation accompanying cyclic martensitic transformation in thermomechanically loaded NiTi. *Int. J. Plast.* **2018**, *111*, 53–71. [CrossRef]
137. Cios, G.; Tokarski, T.; Żywczak, A.; Dziurka, R.; Stępień, M.; Marciszko, M.; Pawłowski, B.; Wieczerzak, K.; Bała, P. The investigation of strain-induced martensite reverse transformation in AISI 304 austenitic stainless steel. *Metall. Mater. Trans. A* **2017**, *48*, 4999–5008. [CrossRef]
138. Cunningham, W.S.; Gentile, J.M.; El-Atwani, O.; Taylor, C.N.; Efe, M.; Maloy, S.A.; Trelewicz, J.R. Softening due to grain boundary cavity formation and its competition with hardening in helium implanted nanocrystalline tungsten. *Sci. Rep.* **2018**, *8*, 1–10. [CrossRef] [PubMed]
139. Fischer, F.D.; Sun, Q.P.; Tanaka, K. Transformation-induced plasticity (TRIP). *Appl. Mech. Rev.* **1996**, *49*, 317–364. [CrossRef]
140. Fischer, F.D.; Reisner, G.; Werner, E.; Tanaka, K.; Cailletaud, G.; Antretter, T. A new view on transformation induced plasticity (TRIP). *Int. J. Plast.* **2000**, *16*, 723–748. [CrossRef]
141. Jacques, P.; Furnémont, Q.; Mertens, A.; Delannay, F. On the sources of work hardening in multiphase steels assisted by transformation-induced plasticity. *Philos. Mag. A* **2001**, *81*, 1789–1812. [CrossRef]
142. Sun, G.S.; Du, L.X.; Hu, J.; Xie, H.; Wu, H.Y.; Misra, R.D.K. Ultrahigh strength nano/ultrafine-grained 304 stainless steel through three-stage cold rolling and annealing treatment. *Mater. Charact.* **2015**, *110*, 228–235. [CrossRef]
143. Knezevic, M.; Levinson, A.; Harris, R.; Mishra, R.K.; Doherty, R.D.; Kalidindi, S.R. Deformation twinning in AZ31: Influence on strain hardening and texture evolution. *Acta Mater.* **2010**, *58*, 6230–6242. [CrossRef]
144. Piao, K.; Chung, K.; Lee, M.G.; Wagoner, R.H. Twinning-slip transitions in Mg AZ31B. *Metall. Mater. Trans. A* **2012**, *43*, 3300–3313. [CrossRef]
145. Sahoo, S.K.; Toth, L.S.; Biswas, S. An analytical model to predict strain-hardening behaviour and twin volume fraction in a profoundly twinning magnesium alloy. *Int. J. Plast.* **2019**, *119*, 273–290. [CrossRef]
146. Sun, J.; Hensel, J.; Klassen, J.; Nitschke-Pagel, T.; Dilger, K. Solid-state phase transformation and strain hardening on the residual stresses in S355 steel weldments. *J. Mater. Process. Technol.* **2019**, *265*, 173–184. [CrossRef]
147. Bay, N. Mechanisms producing metallic bonds in cold welding. *Weld. J.* **1983**, *62*, 137.
148. Ueji, R.; Fujii, H.; Cui, L.; Nishioka, A.; Kunishige, K.; Nogi, K. Friction stir welding of ultrafine grained plain low-carbon steel formed by the martensite process. *Mater. Sci. Eng. A* **2006**, *423*, 324–330. [CrossRef]
149. Kanayama, K.; Tasaki, Y.; Machida, M.; Kume, S.; Aoki, S. Joining of ceramics by friction welding. *Trans. Jpn. Weld. Soc.* **1985**, *16*, 95–96.

150. Gao, J.; Wang, K.; Fu, X.; Chen, S.; Zhang, Z.; Wang, Q.; Li, J.; Yu, Q. Super plasticity in a cold-welded Al-Cu joint. *Appl. Phys. Lett.* **2019**, *114*, 063101. [CrossRef]
151. Maehara, Y.; Langdon, T.G. Superplasticity in ceramics. *J. Mater. Sci.* **1990**, *25*, 2275–2286. [CrossRef]
152. Carry, C.; Mocellin, A. Structural superplasticity in single phase crystalline ceramics. *Ceram. Int.* **1987**, *13*, 89–98. [CrossRef]
153. Perevezentsev, V.N.; Rybin, V.V.; Chuvil'Deev, V.N. The theory of structural superplasticity—I. The physical nature of the superplasticity phenomenon. *Acta Metall. Mater.* **1992**, *40*, 887–894. [CrossRef]
154. Cao, W.; Huang, C.; Wang, C.; Dong, H.; Weng, Y. Dynamic reverse phase transformation induced high-strain-rate superplasticity in low carbon low alloy steels with commercial potential. *Sci. Rep.* **2017**, *7*, 9199. [CrossRef] [PubMed]
155. Perrillat, J.P.; Chantel, J.; Tauzin, B.; Jonfal, J.; Daniel, I.; Jing, Z.; Wang, Y. Acoustic Velocities Across the Olivine-Wadsleyite-Ringwoodite Transitions and the Seismic Signature of the 410 km Mantle Discontinuity. In Proceedings of the AGUFM 2017, New Orleans, LA, USA, 11–15 December 2017. DI13A-0279.
156. Cao, Y.; Du, J.; Park, M.; Jung, S.; Park, Y.; Kim, D.; Choi, S.; Jung, H.; Austrheim, H. Metastability and nondislocation-based deformation mechanisms of the Flem eclogite in the Western Gneiss Region, Norway. *J. Geophys. Res. Solid Earth* **2020**, *125*, e2020JB019375. [CrossRef]
157. Bai, Z.; Balbus, G.H.; Gianola, D.S.; Fan, Y. Mapping the kinetic evolution of metastable grain boundaries under non-equilibrium processing. *Acta Mater.* **2020**, *200*, 328–337. [CrossRef]
158. Gordon, R.B. Observation of crystal plasticity under high pressure with applications to the Earth's mantle. *J. Geophys. Res.* **1971**, *76*, 1248–1254. [CrossRef]
159. Sammis, C.G.; Dein, J.L. On the possibility of transformational superplasticity in the earth's mantle. *J. Geophys. Res.* **1974**, *79*, 2961–2965. [CrossRef]
160. Poirier, J.-P. Martensitic olivine-spinel transformation and plasticity of the mantle transition zone. *Anelast. Earth* **1981**, *4*, 113–117.
161. Reynard, B.; Petit, P.E.; Guyot, F.; Gillet, P. Pressure-induced structural modifications in Mg_2GeO_4-olivine: A Raman spectroscopic study. *Phys. Chem. Mineral.* **1994**, *20*, 556–562. [CrossRef]
162. Sakamoto, H. Distinction between Thermal and Stress-Induced Martensitic Transformations and Inhomogeneity in Internal Stress. *Mater. Trans.* **2002**, *43*, 2249–2255. [CrossRef]
163. Rios, P.R.; Guimarães, J.R.C. Athermal Martensite Transformation Curve. *Mater. Res.* **2016**, *19*, 490–495. [CrossRef]
164. Ferrand, T.P. Neither antigorite nor its dehydration is "metastable". *Am. Mineral. J. Earth Planet. Mater.* **2019**, *104*, 788–790. [CrossRef]
165. Frohlich, C. The nature of deep-focus earthquakes. *Annu. Rev. Earth Planet. Sci.* **1989**, *17*, 227. [CrossRef]
166. Guyot, F.; Gwanmesia, G.D.; Liebermann, R.C. An olivine to beta phase transformation mechanism Mg_2SiO_4. *Geophys. Res. Lett.* **1991**, *18*, 89–92. [CrossRef]
167. Chen, J.; Weidner, D.J.; Parise, J.B.; Vaughan, M.T.; Raterron, P. Observation of cation reordering during the olivine-spinel transition in fayalite by in situ synchrotron X-ray diffraction at high pressure and temperature. *Phys. Rev. Lett.* **2001**, *86*, 4072. [CrossRef]
168. Raterron, P.; Chen, J.; Weidner, D.J. A process for low-temperature olivine-spinel transition under quasi-hydrostatic stress. *Geophys. Res. Lett.* **2002**, *29*, 36-1–36-4. [CrossRef]
169. Chernenko, V.A.; Besseghini, S.; Kanomata, T.; Yoshida, H.; Kakeshita, T. Effect of high hydrostatic pressure on premartensitic transition in Ni_2MnGa. *Scr. Mater.* **2006**, *55*, 303–306. [CrossRef]
170. Chernenko, V.A.; Pons, J.; Seguı, C.; Cesari, E. Premartensitic phenomena and other phase transformations in Ni-Mn-Ga alloys studied by dynamical mechanical analysis and electron diffraction. *Acta Mater.* **2002**, *50*, 53–60. [CrossRef]
171. Perrillat, J.-P.; Chollet, M.; Durand, S.; van de Moortèle, B.; Chambat, F.; Mezouar, M.; Daniel, I. Kinetics of the olivine-ringwoodite transformation and seismic attenuation in the Earth's mantle transition zone. *Earth Planet. Sci. Lett.* **2016**, *433*, 360–369. [CrossRef]
172. Perrillat, J.-P.; Daniel, I.; Bolfan-Casanova, N.; Chollet, M.; Morard, G.; Mezouar, M. Mechanism and kinetics of the α-β transition in San Carlos olivine $Mg_{1.8}Fe_{0.2}SiO_4$. *J. Geophys. Res. Solid Earth* **2013**, *118*, 110–119. [CrossRef]
173. Rosa, A.D.; Hilairet, N.; Ghosh, S.; Perrillat, J.P.; Garbarino, G.; Merkel, S. Evolution of grain sizes and orientations during phase transitions in hydrous Mg_2GeO_4. *J. Geophys. Res. Solid Earth* **2016**, *121*, 7161–7176. [CrossRef]
174. Leinenweber, K.; Utsumi, W.; Tsuchida, Y.; Yagi, T.; Kurita, K. Unquenchable high-pressure perovskite polymorphs of $MnSnO_3$ and $FeTiO_3$. *Phys. Chem. Mineral.* **1991**, *18*, 244–250. [CrossRef]
175. Kanzaki, M.; Xue, X. Protoenstatite in $MgSiO_3$ samples prepared by conventional solid-state reaction. *J. Mineral. Petrol. Sci.* **2017**, *112*, 170616. [CrossRef]
176. Gardés, E.; Gaillard, F.; Tarits, P. Toward a unified hydrous olivine electrical conductivity law. *Geochem. Geophys. Geosyst.* **2014**, *15*, 4984–5000. [CrossRef]
177. Sarafian, E.; Evans, R.L.; Collins, J.A.; Elsenbeck, J.; Gaetani, G.A.; Gaherty, J.B.; Hirth, G.; Lizarralde, D. The electrical structure of the central Pacific upper mantle constrained by the NoMelt experiment. *Geochem. Geophys. Geosyst.* **2015**, *16*, 1115–1132. [CrossRef]
178. Matsuno, T.; Seama, N.; Evans, R.L.; Chave, A.D.; Baba, K.; White, A.; Goto, T.-N.; Heison, G.; Boren, G.; Yoneda, A.; et al. Upper mantle electrical resistivity structure beneath the central Mariana subduction system. *Geochem. Geophys. Geosyst.* **2010**, *11*. [CrossRef]

179. Evans, R.L.; Sarafian, E.; Sarafian, A.R. The Evolution of the Oceanic Lithosphere: An Electromagnetic Perspective. In *Lithospheric Discontinuities*; American Geophysical Union: Washington, DC, USA, 2018; pp. 35–53.
180. Chanard, K.; Fleitout, L.; Calais, E.; Barbot, S.; Avouac, J.P. Constraints on transient viscoelastic rheology of the asthenosphere from seasonal deformation. *Geophys. Res. Lett.* **2018**, *45*, 2328–2338. [CrossRef]
181. Thielmann, M.; Rozel, A.; Kaus, B.J.P.; Ricard, Y. Intermediate-depth earthquake generation and shear zone formation caused by grain size reduction and shear heating. *Geology* **2015**, *43*, 791–794. [CrossRef]
182. Yoshida, H.; Morita, K.; Kim, B.N.; Matsui, K.; Ikuhara, Y.; Sakuma, T. Improvement of Superplasticity in Fine-Grained Oxide Ceramics Based on the Concept of Grain Boundary Plasticity. In *Materials Science Forum*; Trans Tech Publications Ltd.: Bach, Switzerland, 2016; Volume 838, pp. 34–40.
183. Hiraga, K.; Kim, B.N.; Morita, K.; Yoshida, H.; Suzuki, T.S.; Sakka, Y. High-strain-rate superplasticity in oxide ceramics. *Sci. Technol. Adv. Mater.* **2007**, *8*, 578. [CrossRef]
184. Hiraga, T.; Miyazaki, T.; Yoshida, H.; Zimmerman, M.E. Comparison of microstructures in superplastically deformed synthetic materials and natural mylonites: Mineral aggregation via grain boundary sliding. *Geology* **2013**, *41*, 959–962. [CrossRef]
185. Précigout, J.; Hirth, G. B-type olivine fabric induced by grain boundary sliding. *Earth Planet. Sci. Lett.* **2014**, *395*, 231–240. [CrossRef]
186. Smith, C.S. Zener pinning. *Trans. Metall. Soc. AIME* **1948**, *175*, 15–51.
187. Tasaka, M.; Hiraga, T.; Zimmerman, M.E. Influence of mineral fraction on the rheological properties of forsterite + enstatite during grain-size-sensitive creep: 2. Deformation experiments. *J. Geophys. Res. Solid Earth* **2013**, *118*, 3991–4012. [CrossRef]
188. Ferrand, T.P.; Labrousse, L.; Eloy, G.; Fabbri, O.; Hilairet, N.; Schubnel, A. Energy balance from a mantle pseudotachylyte, Balmuccia, Italy. *J. Geophys. Res. Solid Earth* **2018**, *123*, 3943–3967. [CrossRef]
189. Jung, H.; Karato, S. Water-induced fabric transitions in olivine. *Science* **2001**, *293*, 1460–1463. [CrossRef]
190. Poirier, J.-P.; Nicolas, A. Deformation-induced recrystallization due to progressive misorientation of subgrains, with special reference to mantle peridotites. *J. Geol.* **1975**, *83*, 707–720. [CrossRef]
191. Miyazaki, T.; Sueyoshi, K.; Hiraga, T. Olivine crystals align during diffusion creep of Earth's upper mantle. *Nature* **2013**, *502*, 321. [CrossRef] [PubMed]
192. Durinck, J.; Legris, A.; Cordier, P. Pressure sensitivity of olivine slip systems: First-principle calculations of generalised stacking faults. *Phys. Chem. Mineral.* **2005**, *32*, 646–654. [CrossRef]
193. Sundberg, M.; Cooper, R.F. Crystallographic preferred orientation produced by diffusional creep of harzburgite: Effects of chemical interactions among phases during plastic flow. *J. Geophys. Res. Solid Earth* **2008**, *113*. [CrossRef]
194. Maruyama, G.; Hiraga, T. Grain-to multiple-grain-scale deformation processes during diffusion creep of forsterite + diopside aggregate: 2. Grain boundary sliding-induced grain rotation and its role in crystallographic preferred orientation in rocks. *J. Geophys. Res. Solid Earth* **2017**, *122*, 5916–5934. [CrossRef]
195. Ferrand, T.P. Reproduction Expérimentale d'Analogues de Séismes Mantelliques par Déshydratation de l'Antigorite et Comparaison à des Pseudotachylites Naturelles. Ph.D. Thesis, Laboratoire de Géologie de l'Ecole Normale Supérieure, PSL Research Unisversity, Paris, France, 2017.
196. Marquardt, K.; Faul, U.H. The structure and composition of olivine grain boundaries: 40 years of studies, status and current developments. *Phys. Chem. Mineral.* **2018**, *45*, 139–172. [CrossRef]
197. Hiraga, T.; Anderson, I.M.; Kohlstedt, D.L. Grain boundaries as reservoirs of incompatible elements in the Earth's mantle. *Nature* **2004**, *427*, 699–703. [CrossRef] [PubMed]
198. Takei, Y. Experimental and theoretical approaches to grain boundary premelting: A possible origin of asthenosphere. *Geophys. Res. Abstr.* **2019**, *21*, 1.
199. Trubienko, O.; Fleitout, L.; Garaud, J.D.; Vigny, C. Interpretation of interseismic deformations and the seismic cycle associated with large subduction earthquakes. *Tectonophysics* **2013**, *589*, 126–141. [CrossRef]
200. Trubienko, O.; Garaud, J.D.; Fleitout, L. Models of postseismic deformation after megaearthquakes: The role of various rheological and geometrical parameters of the subduction zone. *Solid Earth Discuss.* **2014**, *6*, 427–466.
201. Dumoulin, C.; Doin, M.P.; Fleitout, L. Heat transport in stagnant lid convection with temperature-and pressure-dependent Newtonian or non-Newtonian rheology. *J. Geophys. Res. Solid Earth* **1999**, *104*, 12759–12777. [CrossRef]
202. Fleitout, L.; Froidevaux, C. Tectonics and topography for a lithosphere containing density heterogeneities. *Tectonics* **1982**, *1*, 21–56. [CrossRef]
203. Pico, T.; Mitrovica, J.X.; Perron, J.T.; Ferrier, K.L.; Braun, J. Influence of glacial isostatic adjustment on river evolution along the US mid-Atlantic coast. *Earth Planet. Sci. Lett.* **2019**, *522*, 176–185. [CrossRef]
204. Paulson, A.; Richards, M.A. On the resolution of radial viscosity structure in modelling long-wavelength postglacial rebound data. *Geophys. J. Int.* **2009**, *179*, 1516–1526. [CrossRef]
205. Fleitout, L.; Froidevaux, C. Tectonic stresses in the lithosphere. *Tectonics* **1983**, *2*, 315–324. [CrossRef]
206. Rubie, D.C. Reaction enhanced deformability. In *Deformation Processes in Minerals, Ceramics & Rocks*; Mineralogical Society, Unwin Hyman: London, UK, 1990; pp. 262–292.
207. Morgan, J.P.; Smith, W.H. Flattening of the sea-floor depth-age curve as a response to asthenospheric flow. *Nature* **1992**, *359*, 524. [CrossRef]

208. Chanard, K. Déformation Saisonnière de la Terre sous L'effet des Variations Hydrologiques et Impact sur la Sismicité. Ph.D. Thesis, Laboratoire de Géologie de l'Ecole Normale Supérieure, Paris, France, 2015.
209. Kaneshima, S.; Okamoto, T.; Takenaka, H. Evidence for a metastable olivine wedge inside the subducted Mariana slab. *Earth Planet. Sci. Lett.* **2007**, *258*, 219–227. [CrossRef]
210. Kawakatsu, H.; Yoshioka, S. Metastable olivine wedge and deep dry cold slab beneath southwest Japan. *Earth Planet. Sci. Lett.* **2011**, *303*, 1–10. [CrossRef]